Miner Deposita (2017) 52:799–821
DOI 10.1007/s00126-016-0702-8

ARTICLE

Mo-mineralized porphyries are relatively hydrous and differentiated: insights from the Permian-Triassic granitic complex in the Baituyingzi Mo–Cu district, eastern Inner Mongolia, NE China

Yan Sun [1,2] · Jianming Liu [3] · Qingdong Zeng [3] · Jingbin Wang [1] · Yuwang Wang [1] · Ruizhong Hu [2] · Lingli Zhou [3] · Guanbin Wu [3]

Received: 10 December 2015 / Accepted: 28 November 2016 / Published online: 9 December 2016

Abstract Mo–Cu mineralization in the Baituyingzi district of eastern Inner Mongolia occurs within a granitic complex. This paper presents and discusses zircon U–Pb ages and whole-rock geochemical and Sr–Nd–Pb isotopic data from the granitic complex as potential indicators for porphyry Mo fertility. The U–Pb ages indicate that five units of the granitic complex were emplaced between 265.2 ± 0.7 and 246.5 ± 1.0 Ma. Constrained by crosscutting dikes, Mo–Cu mineralization was probably related to the Baituyingzi monzogranite porphyry dated at 248.2 ± 0.64 Ma. The intrusions belong to high-K calc-alkaline to shoshonitic series that are characterized by highly fractionated rare earth element (REE) patterns and strong enrichments of large ion lithophile elements, relative to high-field strength elements. Apart from the ~246-Ma dike that shows negative εNd (t) values (−14.9 to −13.1), the intrusions have εNd(t) values ranging from −3.9 to 1.0, relatively young depleted mantle model ages (811 to 1183 Ma), $^{206}Pb/^{204}Pb$ of 18.137–18.335, and $^{207}Pb/^{204}Pb$ of 15.591–15.625, which are consistent with a juvenile lower crustal origin. Among the intrusions, the ~248-Ma porphyry and the ~246-Ma dike show adakite-like characteristics (e.g., Sr/Y = 44.9–185) and listric-shaped REE patterns that indicate amphibole fractionation and a hydrous magma source. However, the porphyry exhibits a higher differentiation index (81.4–91.5) and a steeper REE profile (e.g., La_N/Yb_N = 25.6–87.0) than those of the ~246-Ma dike, which suggests that it is highly differentiated. We propose that the complex was generated by the partial melting of juvenile mafic lower crust (containing minor old crustal relicts) that was triggered by collision between the North China Craton and Siberian Craton. As indicated by the Th/Nb, Th/Yb, Ba/Th, and Ba/La ratios of the intrusions, the crust may have been derived from the melting of the fertile mantle wedge that was metasomatized by various amounts of slab-derived fluids or melts due to earlier subduction and was heterogeneous in terms of water, Cu, Mo, and S contents and possible oxidation state. The fertility of the porphyry was likely associated with the addition of earlier subduction-related slab melts to the magma source (leading to a hydrous and possible high oxidation state) and the long-time (~20 Ma) collision tectonic setting in which it formed (resulting in a highly differentiated state).

Keywords Xilamulun Mo belt · Baituyingzi porphyry Mo–Cu district · U–Pb dating · Sr–Nd–Pb isotopes · Mo-related granitic complex · Geochemistry · Editorial handling: T. Bissig

Editorial handling: T. Bissig

Electronic supplementary material The online version of this article (doi:10.1007/s00126-016-0702-8) contains supplementary material, which is available to authorized users.

✉ Yan Sun
825143846@qq.com

[1] Beijing Institute of Geology for Mineral Resources, Beijing 100012, China

[2] Institute of Geochemistry, Chinese Academy of Sciences, Guiyang 550002, China

[3] Key Laboratory of Mineral Resources, Institute of Geology and Geophysics, Chinese Academy of Sciences, Beijing 100029, China

Introduction

Porphyry deposits are the most important sources of Cu and Mo globally, and they account for approximately 60 to 70% of global Cu production and more than 95% of global Mo

production (Sinclair 2007; Sillitoe 2010). Metals (e.g., Cu and Mo) in porphyry deposits are derived predominantly from magmatic-hydrothermal fluids that exsolved following the emplacement of felsic to intermediate magmas in the middle to upper crust (e.g., Richards 2003, 2011a; Seedorff et al. 2005; Audétat 2010). Generally, the magmatic intrusive activity in a given region occurs as a multiphase intrusive complex or as widely distributed coeval intrusions; therefore, distinguishing between barren and mineralized intrusions in a given district is crucial for exploration (e.g., Seedorff et al. 2005; Sillitoe 2010; Richards et al. 2012).

Factors determining the Cu (Mo)-mineralizing potential of granitic intrusions include age, oxidation state, water content, and sulfur fugacity of the magmatic source (e.g., Mungall 2002; Macpherson et al. 2006); the mixing of mafic material in the rising magma (e.g., Hattori and Keith 2001; Stavast et al. 2006; Hou et al. 2013); and the size of the magma chamber, emplacement, and degassing pattern of the magma, as well as the degree of fluid focusing (e.g., Audétat 2010; Richards 2011a; Lerchbaumer and Audétat 2013). Although these factors are quite complicated and include the whole origin and evolutionary process of the magma, numerous mineralogical, petrologic, and geochemical studies of intrusions in porphyry Cu systems reveal that it may be possible to distinguish fertile from barren intrusions via characteristic geochemical indexes. The results from these studies commonly show that ore-forming silicic magmas were oxidized (e.g., zircons yielding $Ce^{4+}/Ce^{3+} > 100$ (Ballard et al. 2002; Liang et al. 2006; Wang et al. 2013; Wang et al. 2014b; Shen et al. 2015) or the existence of magmatic anhydrite (Audétat and Pettke 2006; Chambefort et al. 2008)), relatively wet (e.g., hornblende and biotite are phenocrystic and dominate over pyroxene in intermediate composition magmas, and the magmas show Sr/Y ratios >20 and listric-shaped rare earth element (REE) patterns (Shafiei et al. 2009; Liu et al. 2010b; Richards 2011b; Wang et al. 2014a)), and differentiated (e.g., as evidenced by trace element compositions (Richards et al. 2012)) in comparison to other apparently barren intrusions in the same district.

However, few data exist concerning the fertile characteristics of intrusions from porphyry Mo deposits (e.g., Qiu et al. 2013), although porphyry Mo deposits exhibit many differences in deposit characteristics, compositions of intrusions and fluids, and tectonic environment compared to porphyry Cu deposits (Carten et al. 1993; Seedorff et al. 2005; Steve and Plumlee 2009; Audétat 2010; Sillitoe 2010; Sun et al. 2012). Additionally, porphyry Mo deposits are mainly found in intraplate extensional settings or continental margin magmatic arcs (e.g., Westra and Keith 1981; Carten et al. 1993; Mao et al. 2005); studies of those forming in collisional orogenic settings are rare (e.g., Qin et al. 2008; Zeng et al. 2012, 2013).

The Xilamulun Mo metallogenic belt, which is approximately 400 km in length and 100–300 km in width, is a recently distinguished Mo–Cu metallogenic belt located within the eastern segment of the well-known Central Asian Orogenic Belt (CAOB; Fig. 1a). The Baituyingzi Mo–Cu system, which was recently discovered by the No. 243 Geological Team of China Nuclear Geology in 2010, is situated in the southern part of the Xilamulun Mo metallogenic belt, Inner Mongolia, NE China (Fig. 1b). The Mo–Cu mineralization occurs within the Baituyingzi granitic complex (Fig. 2). Currently, reserves of Cu and Mo in the Baituyingzi district are >140,000 and >80,000 t, respectively. Molybdenite Re–Os dating confirmed that the mineralization occurred in the Early Triassic period (248–245 Ma; Sun et al. 2013) and probably formed during the collision between the North China Craton (NCC) and Siberian Craton (SC). This paper presents the integrated results from zircon U–Pb geochronology by laser ablation inductively coupled plasma mass spectrometry (LA-ICP-MS) together with geochemical and Sr–Nd–Pb isotope data from the granitic complex in the Baituyingzi district. Our main objectives were to (1) investigate the timing and tectonic setting of the magma activity and Mo–Cu mineralization in the Baituyingzi district and (2) identify the distinguishing features of ore-related intrusions and explore their possible origins. Based on these results, we attempt to establish the genetic model of Mo porphyries.

Regional geology and deposit geology

Geology of the Xilamulun Mo belt

The tectonic framework of the Xilamulun Mo belt, including the northern margin of the NCC, was predominantly shaped by the following two major events: subduction and accretion of the Paleo-Asian Ocean during the Paleozoic and intracontinental extensional events triggered by subduction of the Pacific Ocean Plate since the late Mesozoic (e.g., Sengör and Natal'in 1996; Windley et al. 2007; Kusky et al. 2007).

From the Neoproterozoic to the Paleozoic, this region is considered to have been an active continental margin associated with southward subduction of the Paleo-Asian Oceanic Plate beneath the NCC along the Chifeng–Bayan Obo Fault, a major lithotectonic boundary separating the NCC and the CAOB (e.g., Jian et al. 2008; Zhang et al. 2009b; Jian et al. 2010; Zhao et al. 2010). This stage was characterized by a series of subduction–collision–accretion events involving multiple island arcs and microcontinents coupled with voluminous intrusive and extrusive magmatism (Sengör and Natal'in 1996; Windley et al. 2007; Jahn et al. 2004; Wu et al. 2011a). The Paleo-Asian Ocean is considered to have ultimately closed along the Solonker–Xilamulun–Jilin–Yanji suture zone between the late Permian and the Middle Triassic, resulting in the amalgamation of the NCC and the SC (Xiao et al. 2003, 2009; Li 2006; Li et al. 2007; Wu et al. 2007; Jian

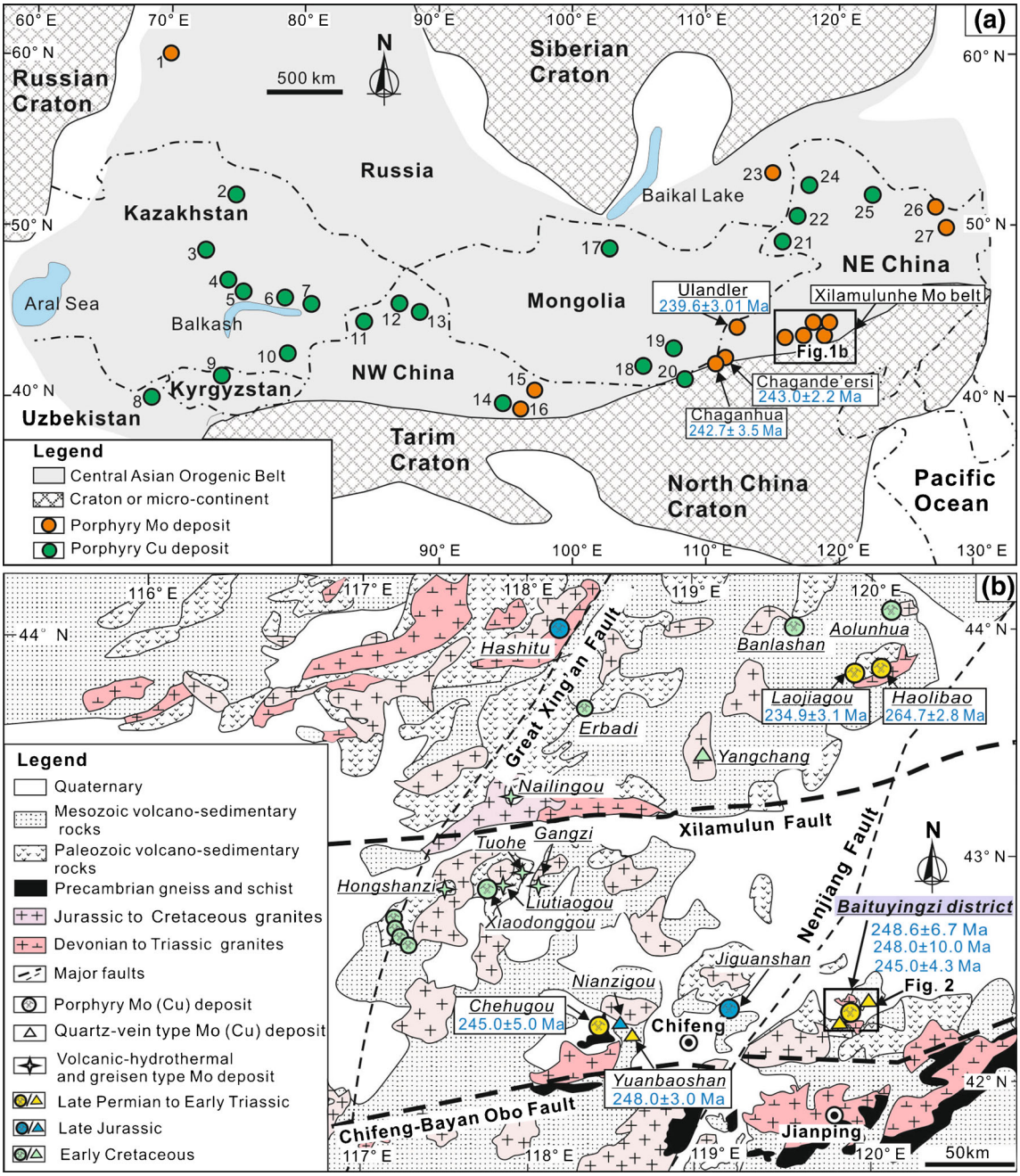

Fig. 1 **a** Sketch tectonic map of the Central Asian Orogenic Belt (CAOB) showing the location of major porphyry Cu and Mo deposits/districts (modified after Mao et al. 2014, Seltmann et al. 2014, and Shen et al. 2015) and **b** geological map of the Xilamulun Mo metallogenic belt (modified from Zeng et al. 2011 and Zhang et al. 2009a). *1* Shameika, *2* Bozshekui, *3* Samarsk, *4* Borly, *5* Kounrad, *6* Sayak, *7* Aktogai, *8* Kal'makyr, *9* Taldy Bulak, *10* Koksai, *11* Baogutu, *12* Xilekuduke, *13* Yulekenhalasu, *14* Tuwu-Yandong, *15* Baishan, *16* Donggebi, *17* Erdenet, *18* Oyu Tologoi, *19* Tsagan-Suvarga, *20* Bainaimiao, *21* Badaguan, *22* Taipingchuan, *23* Shakhtama, *24* Wulugetushan, *25* Duobaoshan, *26* Luming, *27* Daheishan. The Mo mineralization ages (late Permian to Middle Triassic) in Fig. 1a, b are molybdenite Re–Os isochron ages corresponding to Table 3

et al. 2010). Subsequent post-collisional/post-orogenic extension and voluminous magmatism prevailed in the region in the Late Triassic (Wu et al. 2002; Davis et al. 2004). During the Mesozoic, this region was intensely influenced by the westward subduction of the Pacific Ocean Plate. Subsequently, tectonic extension and lithospheric thinning occurred widely throughout this region (Wu et al. 2002; Kusky et al. 2007).

The strata exposed are dominated by Paleozoic arc volcano-sedimentary assemblages and Mesozoic continental volcano-sedimentary successions. The regional structures are characterized by a series of approximately E striking faults that are cut by NE striking faults (Fig. 1b). Late Paleozoic to late Mesozoic granitoids occur widely along the major faults (Fig. 1b). They are dominated by granite, monzonitic granite,

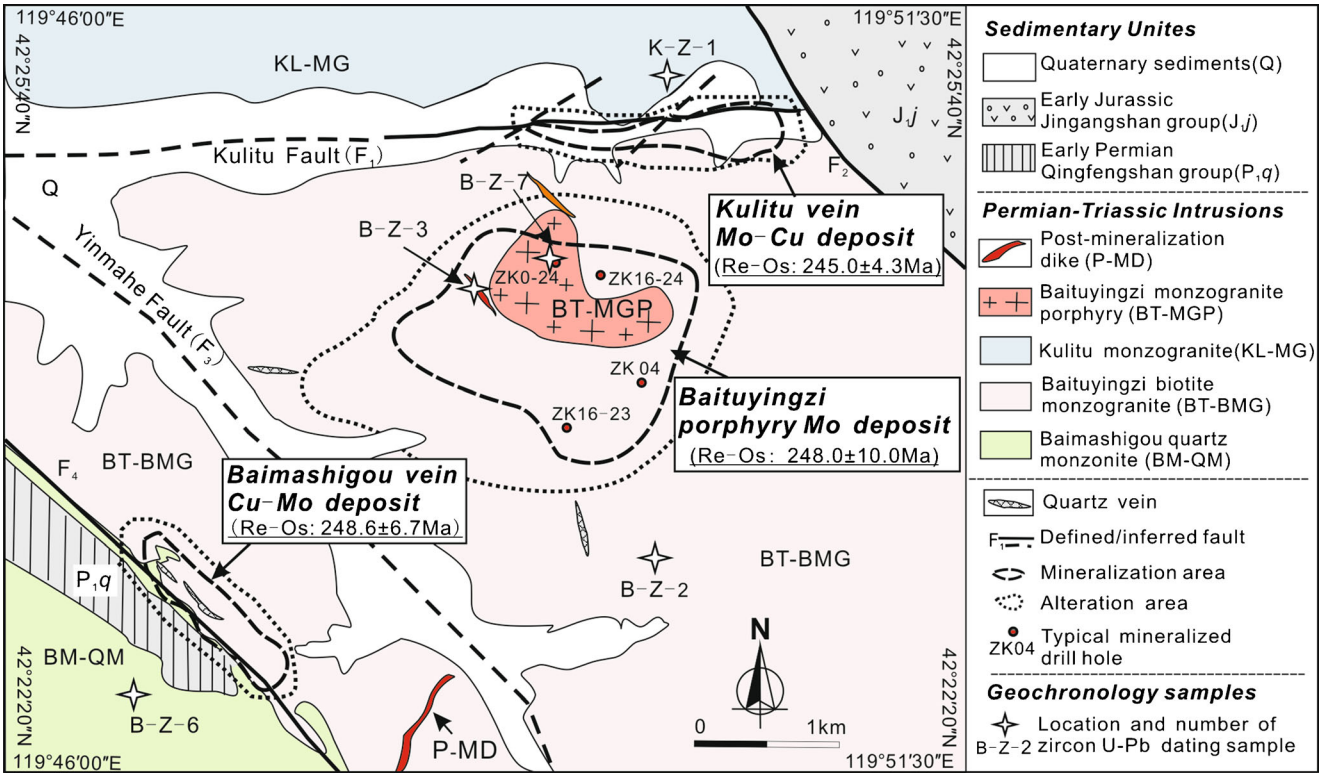

Fig. 2 Geological map of the Baituyingzi district in Inner Mongolia, showing locations of zircon U–Pb dating samples from intrusions and earlier molybdenite Re–Os isochron ages for the three Mo (−Cu) deposits (after Sun et al. 2013)

quartz porphyry, granite porphyry, syenite, and syenite porphyry, and the latter four types host Mo mineralization in this district. Consistent with the majority of Phanerozoic granitoids in the CAOB, most of the Phanerozoic granites in this region are characterized by positive $\varepsilon Nd(t)$ values, implying an important mantle-derived component in these magmas (Jahn et al. 2000, 2004; Wu et al. 2005, 2011a). However, some evidence indicates that the source of several granitoids also includes some reworking of older components (Liu et al. 2005; Wu et al. 2011a; Li et al. 2012).

More than 10 medium- (0.01–0.1 Mt Mo) to large-sized (0.1–0.5 Mt Mo) Mo (−Cu) deposits have been found in the Xilamulun Mo belt (Fig. 1b), including the following three major types: porphyry (e.g., the Chehugou, Baituyingzi, Xiaodonggou, and Jiguanshan Mo–Cu deposits), quartz vein (e.g., the Nianzigou and Yangchang Mo deposits), and volcanic-hydrothermal (e.g., the Hongshanzi Mo–U deposit) (Chen et al. 2008; Qin et al. 2009; Wan et al. 2009; Zhang et al. 2009a; Wu et al. 2011b; Zeng et al. 2011, 2012, 2013, 2014; Sun et al. 2013; Duan et al. 2015). Geochronologic studies show that the Mo mineralization in the Xilamulun belt occurred during three main episodes: (1) late Permian to Middle Triassic (265–235 Ma, e.g., the Chehugou Mo–Cu deposit; Liu et al. 2010a; Wan et al. 2009; Zeng et al. 2012; Duan et al. 2015), (2) Late Jurassic (160–150 Ma, e.g., the Jiguanshan Mo deposits; Wu et al. 2011b), and (3) Early Cretaceous (140–142 Ma, e.g., the Yangchang Mo deposit; Zeng et al. 2014).

Geology of the Baituyingzi Mo–Cu district

Permian and Jurassic volcano–sedimentary rocks are only locally distributed in the Kulitu and Baimashigou deposits (Fig. 2). At least three sets of faults and fractures are observed throughout the Baituyingzi district, E, NW, and NE striking faults. Of these, the E trending Kulitu Fault (dipping 50°S) and the NW striking Yinmahe Fault (dipping 50–75°NE) are the most important regional structures and have served as first-order controls on the geometry of ore bodies in the Kulitu and Baituyingzi deposits, respectively.

Extensive magmatic activity occurred in Baituyingzi from the late Permian to the Early Triassic, resulting in the emplacement of the Baituyingzi intrusive complex (Fig. 2). Based on crosscutting relationships in the field (Fig. 3) and petrographic observations, at least five felsic–intermediate intrusions can be distinguished from the complex (from oldest to youngest): (1) Baimashigou quartz monzonite (BM–QM), (2) Baituyingzi biotite monzogranite (BT–BMG), (3) Kulitu monzogranite (KL–MG), (4) Baituyingzi monzogranite porphyry (BT–MGP), and (5) post-mineralization dike (P–MD). All of these intrusions are granitic in composition; porphyritic to granitic in texture; and composed mainly of plagioclase, K-feldspar, quartz, amphibole, and biotite, with accessory minerals represented by titanite, magnetite, apatite, and zircon (Table 1 and Fig. 3).

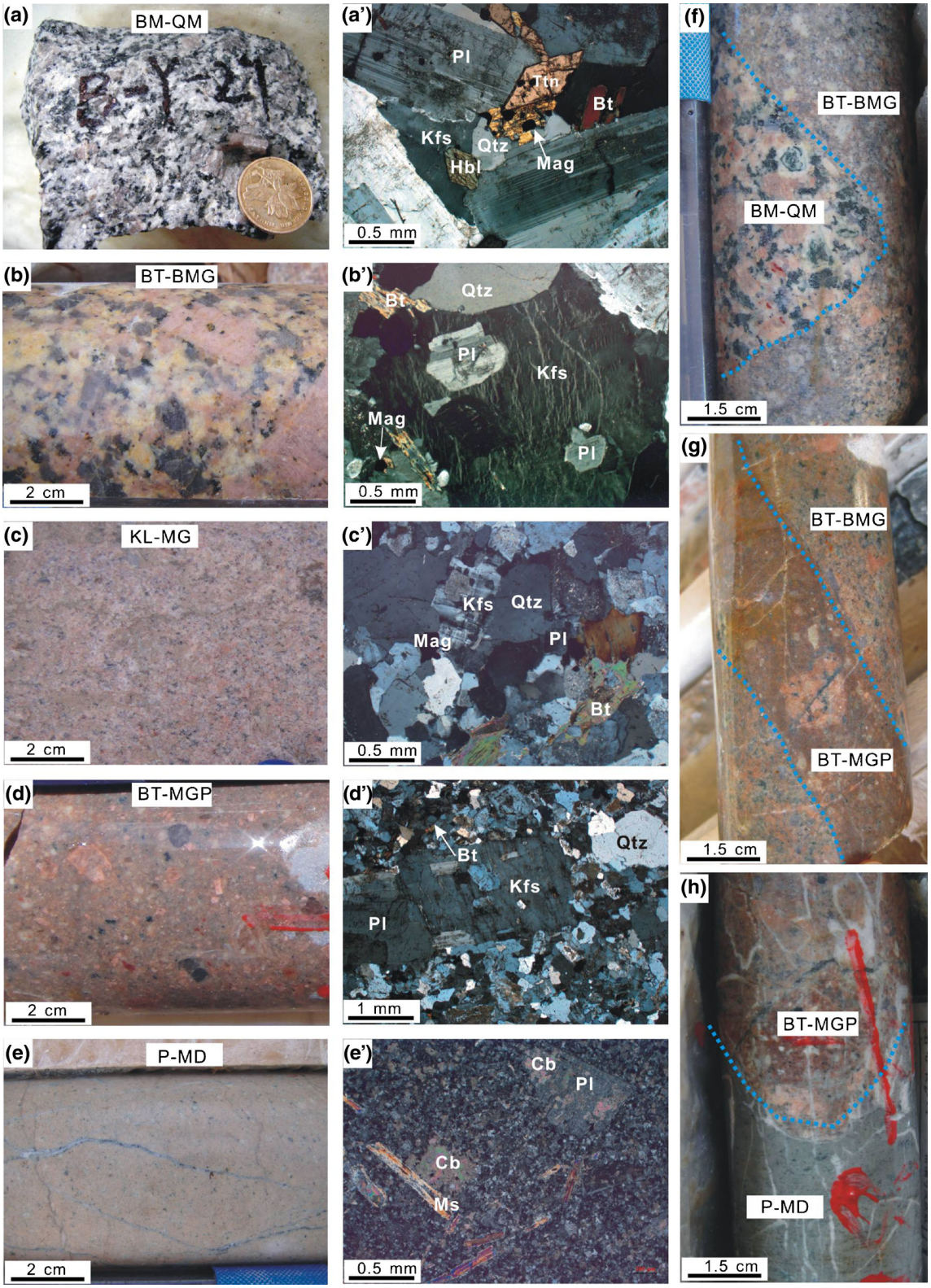

Fig. 3 Photographs and photomicrographs of intrusions in the Baituyingzi Mo-Cu district, Inner Mongolia. **a**, **a′** Baimashigou quartz monzonite (BM–QM). **b**, **b′** Baituyingzi biotite monzogranite (BT–BMG). **c**, **c′** Kulitu monzogranite (KL–MG). **d**, **d′** Baituyingzi monzogranite porphyry (BT–MGP). **e**, **e′** Post-mineralization dike (P–MD). **f** Xenolith of BM–QM in BT–BMG. **g** BT–MGP dike in BT–BMG. **h** Contact relationship between P–MD and BT–MGP. All photomicrographs are under transmitted light. *Bt* biotite, *Cb* carbonate, *Hbl* hornblende, *Kfs* K-feldspar, *Mag* magnetite, *Ms* muscovite, *Pl* Plagioclase, *Qtz* quartz, *Ttn* titanite

Table 1 Petrographic characteristics of major intrusions in the Baituyingzi Mo–Cu district, Inner Mongolia

Rock	Occurrence	Color	Texture	Mineral composition		Alteration	Mineralization
				Major mineral	Accessory mineral		
Baimashigou quartz monzonite (BM–QM)	Batholith	Dark gray	Porphyritic-like, (phenocryst 15–20%)	Phenocryst (10–20 mm), zoned plagioclase; groundmass (0.5–5 mm), plagioclase (10–15%), hornblende (8–10%), K-feldspar (15–20%), quartz (15–20%) and minor biotite (3–5%)	3–5%, titanite, apatite, zircon, and magnetite	Fresh (locally propylitic alteration)	Barren
Baituyingzi biotite monzogranite (BT–BMG)	Batholith	Gray to pink	Porphyritic-like or medium- to coarse-grained granitic (0.5–20 mm)	Zoned plagioclase (25–30%), K-feldspar (20–25%), anhedral quartz (25–30%), biotite (8–10%), and minor hornblende (3–5%)	2–3%, titanite, apatite, zircon, and magnetite	Variable degree of potassic, sericitic, and propylitic alteration	Strong Mo–Cu
Kulitu monzogranite (KL–MG)	Batholith	Pink	Fine- to medium- grained granitic (0.2–2 mm)	Plagioclase (20–25%), microcline (25–30%), quartz (25–30%), and minor biotite	<1%, titanite, apatite, zircon, and magnetite	Fresh (locally sericitic and propylitic alteration)	Barren
Baituyingzi monzogranite porphyry (BT–MGP)	Stock	Pink	Porphyritic (phenocryst 20–25%)	Phenocrysts subhedral K-feldspar (5–10 mm, 5–10%), subrounded quartz (2–5 mm, 5–10%), plagioclase (5–10 mm, 5–10%), and minor biotite and hornblend; groundmass fine-grained quartz, K-feldspar, plagioclase, and minor biotite and hornblend	<1%, titanite, apatite (abundant), zircon, and magnetite	Pervasively potassic and sericitic alteration	Intense Mo
Post-mineralization dike (P–MD)	Dike	Gray to light gray	Porphyritic (phenocryst 15–20%)	Phenocrysts (1–2 mm), plagioclase, biotite, K-feldspar, and quartz; groundmass aplitic quartz, K-feldspar, plagioclase, and minor biotite	Not found	Late carbonation	Barren

Baimashigou quartz monzonite The BM–QM is the earliest intrusion and intruded into the Qingfengshan group in the western part of the Baimashigou quartz vein Cu–Mo deposit (Fig. 2). It is relatively fresh and only weakly affected by propylitic alteration near the F_4 fault.

Baituyingzi biotite monzogranite The BT–BMG is the volumetrically largest intrusion in this district (Fig. 2). Drill hole observations indicate that the BM–QM clearly occurs as angular xenoliths in the BT–BMG (Fig. 3f). On a regional scale, this intrusion is a NW striking batholith with an outcrop area of >155 km^2, and it probably comprises several phases, with rock types ranging from hornblende quartz monzonite to biotite monzogranite. It is the major host of the Mo–Cu mineralization in the Baituyingzi district and is variably affected by potassic, sericitic, quartz, and propylitic alteration (see below).

Kulitu monzogranite The KL–MG crops out in the northern part of the Kulitu quartz vein Mo–Cu deposit (Fig. 2). No clear crosscutting relationships have been observed between the KL–MG and other intrusions. It is barren and only slightly altered to quartz–sericite and propylitic assemblages near the Kulitu fault.

Baituyingzi monzogranite porphyry The BT–MGP occurs as an irregular NW-elongated stock that intruded into the BT–BMG in the central part of the Baituyingzi porphyry Mo deposit (Figs. 2 and 3g). It dips 70–80°SW, has a strike length of approximately 1 km, and varies in width from 300 to 700 m. This porphyry is a compositionally variable unit, with phenocrysts range from K-feldspar and quartz to plagioclase. Compared to the other intrusions, apatite is more common in the BT–MGP, and it occurs both as phenocrysts and in the groundmass.

Another distinctive feature of the BT–MGP is the occurrence of abundant unidirectional solidification texture (UST) quartz and K-feldspar–quartz pegmatite on the northern margins (Fig. 4g, h), implying that the BT–MGP was rich in volatiles during the late stage of its evolution (Harris et al. 2004; Seedorff et al. 2005). In areas adjacent to the contacts between the BT–BMG and the BT–MGP, this stock is pervasively altered to potassic and quartz–sericite assemblages and accompanied by intense Mo mineralization related to quartz vein stockworks.

Post-mineralization dike P–MD rocks are exposed as small, variably striking, discontinuous porphyry dikes that are commonly 0.5 to 50 m wide and cut all other intrusions (Fig. 2). They are essentially unaffected by alteration and sulfide mineralization except for local overprinting by late carbonation. In many drill cores, these dikes truncate the strongly mineralized BT–MGP, thus providing convincing evidence that the P–MD post-dates the main Mo–Cu mineralization in the Baituyingzi district (Fig. 3h).

Moreover, quartz veins are extensively present in the ore district, with orientations clearly following the major faults (Fig. 2). They are usually 0.5–2 m in width and range from 2 to over 100 m in length. Several quartz veins from the Kulitu and Baimashigou deposits serve as hosts to Mo–Cu mineralization.

Deposit geology

Three Mo (Cu) deposits, hosted by the Baituyingzi intrusive complex, occur in this district from NE to SW as follows (Fig. 2): (1) the Kulitu quartz vein Mo–Cu deposit, (2) the Baituyingzi porphyry Mo deposit, and (3) the Baimashigou quartz vein Cu–Mo deposit.

Baituyingzi porphyry Mo deposit

The Baituyingzi porphyry Mo deposit lies at the center of the Baituyingzi district (Fig. 2). According to the latest exploration results, the Mo reserve at Baituyingzi is over 0.05 Mt (average grade 0.14% Mo). In addition, significant Cu, Pb, Zn, and Ag mineralization is locally present, although no resource figures are available on these metals.

Hydrothermal alteration in Baituyingzi is extensively developed and surrounds the BT–MGP stock in the shape of an irregular ellipse, occupying an area of more than 4 km^2. Recognized alteration assemblages are dominated by K-feldspar, sericite, quartz, chlorite, illite, hematite, calcite, and kaolinite. Based on detailed observations, the alteration can be divided into a potassic alteration zone (K-feldspar + quartz ± hematite), a phyllic alteration zone (quartz + sericite + illite ± kaolinite), and a propylitic alteration zone (chlorite + calcite ± hematite) from the BT–MGP stock center outward and upward.

The bulk of the Mo mineralization forms a bell shape that has a diameter of ~1.5 km (Fig. 2) and extends more than 550 m below the surface. The Mo mineralization is confined to the irregular contact zones between the BT–MGP and the BT–BMG, primarily in the form of veinlets (Fig. 4a) and stockwork veinlets (Fig. 4b) related to potassic alteration. Molybdenite and pyrite are the dominant ore minerals, followed by minor amounts of chalcopyrite, magnetite, bornite, and hematite. Molybdenite generally occurs as flakes that are 0.05–0.5 cm in diameter.

Baimashigou quartz vein Cu–Mo deposit

The Baimashigou quartz vein Cu–Mo deposit is situated on the southern margin of the BT–BMG (Fig. 2). It contains 143,000 t of Cu and 22,000 t of Mo (average grade 0.49% Cu, 0.075% Mo; Ma and Li personal communications 2006).

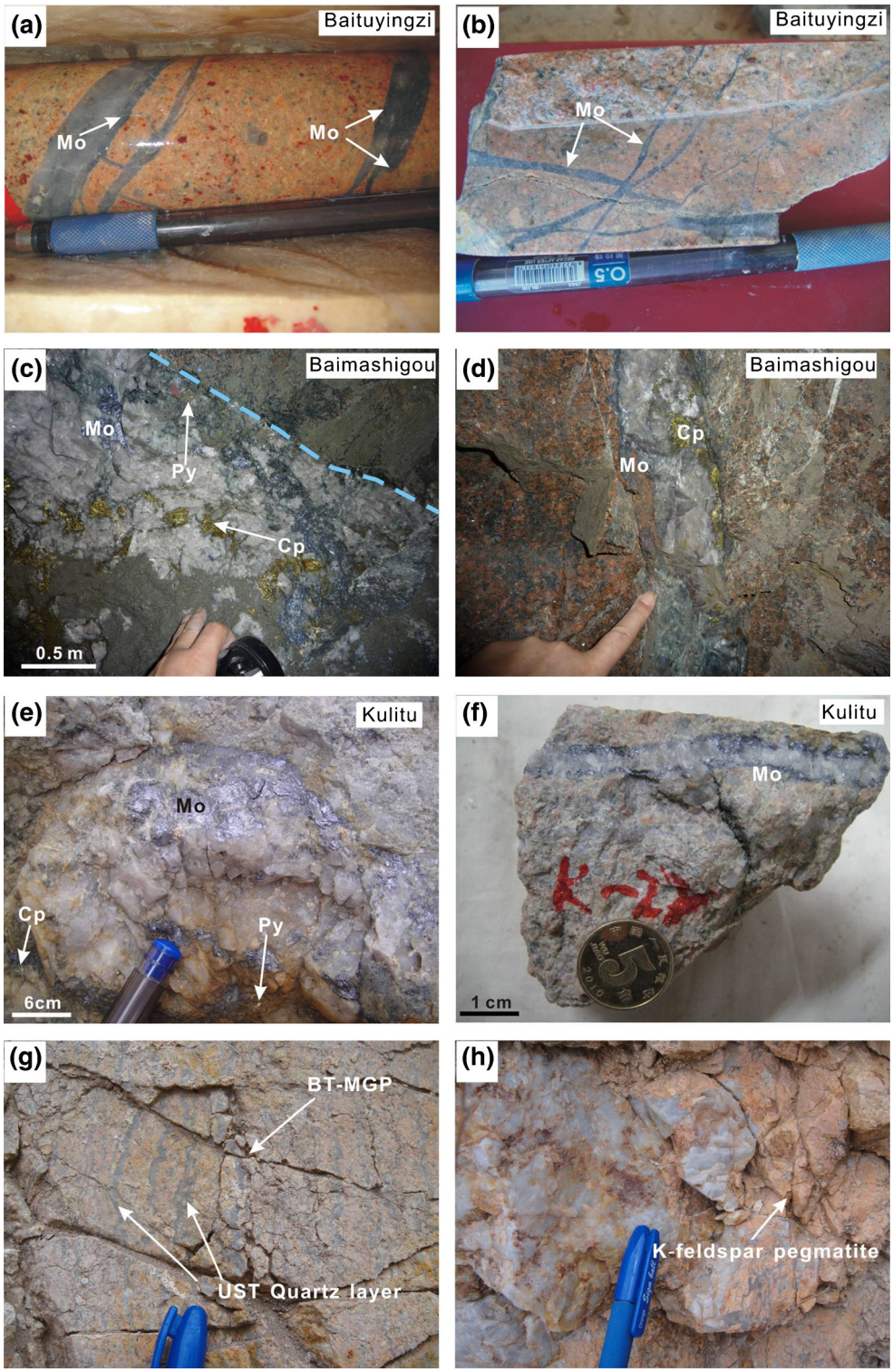

Fig. 4 Representative mineralization types and evidence for a magma-hydrothermal transition at the three deposits in the Baituyingzi Mo–Cu district, Inner Mongolia. **a**, **b** Mineralization style of Baituyingzi, veinlet (**a**) and stockwork (**b**). **c**, **d** Mineralization style of Baimashigou, quartz vein (**c**) and quartz veinlet (**d**). **e**, **f** Mineralization style of Kulitu, quartz vein (**e**) and quartz veinlet (**f**). **g** Unidirectional solidification texture quartz in the BT–MGP, which is direct evidence of fluid exsolution. **h** K-feldspar–quartz pegmatite from the BT–MGP, demonstrating that the monzonite granite porphyry was rich in volatiles during a late stage of evolution. *Cp* chalcopyrite, *Mo* molybdenite, *Py* pyrite

Unlike the Baituyingzi deposit, the alteration and accompanying Cu–Mo mineralization at Baimashigou are chiefly found along the NW trending F_4 fault between the BT–BMG and the BM–QM, extending approximately 1.3 km in length and 0.5 km in width. Apart from quartz, K-feldspar, hematite, chlorite, and carbonate, alteration minerals spatially related to mineralization comprise a significant amount of biotite.

Four major Cu–Mo ore bodies have been discovered at Baimashigou. The occurrences of ore bodies primarily follow the F_4 fault. They generally dip 60–85°NE, have a strike length of 50–300 m, and vary in width from 1 to 17 m. Cu–Mo mineralization in Baimashigou occurs mainly as quartz–sulfide veins (0.1–1 m in width; Fig. 4c) and veinlets (0.5–2 cm in width; Fig. 4d). The ore minerals are composed

primarily of chalcopyrite, molybdenite, pyrite, magnetite, bornite, and hematite. Chalcopyrite and molybdenite generally occur as massive aggregates and flakes (0.3–1 cm in diameter) within fractures in the quartz veins, respectively.

Kulitu quartz vein type Mo–Cu deposit

The Kulitu quartz vein Mo–Cu deposit is located on the northern margin of the BT–BMG (Fig. 2), with Cu + Mo reserves of >10,000 t (average grade 0.09% Mo, 0.4% Cu; Zhang et al. personal communications 2006). Similar to the Baituyingzi deposit, its alternation assemblages include quartz, K-feldspar, sericite, chlorite, and carbonate. However, the alteration zones at Kulitu are constricted to form an E striking belt along the Kulitu fault, which extends for a length of approximately 1.5 km and ranges in width from 0.1 to 0.5 km.

More than ten Mo–Cu ore bodies have been identified at Kulitu, which are dominantly controlled by the E striking Kulitu fault and its secondary NE trending faults and occur as steep S dipping (40°–60°) lenses and veins. Individual ore bodies usually vary in width from 1 to 5 m. The Mo–Cu mineralization in Kulitu occurs mainly in the form of quartz–sulfide veins (0.1–1.5 m in width; Fig. 4e) and veinlets (0.3–1 cm in width; Fig. 4f). Ore minerals comprise primarily flaky molybdenite (0.1–0.8 cm in diameter), chalcopyrite, pyrite and minor magnetite, bornite, and hematite.

Sampling and analytical methods

The granitoid samples in this study were mainly collected from drill cores and outcrops in the Baituyingzi district and broadly represent the compositional range of the five intrusive units. Five samples were chosen for zircon LA-ICP-MS U–Pb dating, and their locations are shown in Fig. 2. To correctly characterize their chemical compositions, 24 whole-rock samples with no visible hydrothermal alteration and weathering were selected for major element and trace element analyses. Of these, 18 samples were analyzed for further Sr–Nd–Pb isotopes. The samples were mainly analyzed at two different laboratories over the duration of the project (see Appendix for detailed methodologies).

Results

Zircon U–Pb ages

The LA-ICP-MS U–Pb analysis results for zircons from intrusions in the Baituyingzi Mo–Cu district are listed in Table S1 and illustrated in Fig. 5.

Zircons from the five samples are moderate to large in size (80–250 μm), prismatic, euhedral, and clearly oscillatory zoned (Fig. 5a–e). Their Th/U ratios range from 0.11 to 1.40 and are all higher than 0.1 (Table S2). These characteristics indicate that they have a magmatic origin (Fernando et al. 2003; Samuel and Mark 2003). Thus, the zircon U–Pb ages can be interpreted as representing the emplacement age of the host rocks. It is worth noting that (1) we chose the $^{206}Pb/^{238}U$ ages to define the rock age considering that the intrusions are relatively young and (2) we used concordia-intercept ages instead of the weighted mean ages of the individual spot analyses to interpret rock ages because concordia diagrams can easily evaluate the possibility for Pb loss, the presence of older zircons, and the influence of common Pb on the interpreted ages (Simmons et al. 2013) and because the concordia intercept age calculated for each sample is generally within analytical uncertainty of the weighted mean $^{206}Pb/^{238}U$ age in our study.

BM–QM Of the 18 zircons from the sample B–Z–6, 15 define a concordant $^{206}Pb/^{238}U$ age of 265.2 ± 0.7 Ma (2σ, mean square weighted deviation (MSWD) = 0.36), which is interpreted as the crystallization age of the BM–QM. Two zircon grains with older $^{206}Pb/^{238}U$ ages (284 ± 3 and 399 ± 3 Ma) are inferred to be xenocrysts, whereas one zircon with a $^{206}Pb/^{238}U$ age of ~258 ± 2 Ma may have undergone some minor Pb loss (Fig. 5 (a′)).

BT–BMG Of the 20 zircons from the sample B–Z–2, 15 define a concordant $^{206}Pb/^{238}U$ age of 255.6 ± 0.68 Ma (2σ, MSWD = 0.014), which is interpreted as the crystallization age of the BT–BMG. The other five zircon grains from B–Z–2, with an older $^{206}Pb/^{238}U$ concordant age of 273.3 ± 1.3 Ma (2σ, MSWD = 0.42), are inferred to be xenocrysts (Fig. 5 (b′)).

Kl–MG Of the 20 zircons from the sample K–Z–1, 18 yield a concordant $^{206}Pb/^{238}U$ age of 252.4 ± 0.69 Ma (2σ, MSWD = 0.116), which is interpreted as the crystallization age of KL–MG. The other two zircon grains with $^{206}Pb/^{238}U$ ages of 300 ± 5 and 276 ± 2 Ma are inferred to be xenocrysts (Fig. 5 (c′)).

BT–MGP Nineteen zircons from the sample B–Z–7 yield a concordant $^{206}Pb/^{238}U$ age of 248.2 ± 0.64 Ma (2σ, MSWD = 0.0084), which is interpreted as the crystallization age of the BT–MGP. No xenocrystic zircons were discovered in this sample (Fig. 5 (d′)).

P–MD Of the 20 zircons from the sample B–Z–3, 13 yield a concordant $^{206}Pb/^{238}U$ age of 246.5 ± 1.0 Ma (2σ, MSWD = 1.6), which is interpreted as the crystallization age of P–MD. The other seven zircons roughly show three groups of older xenocrystic zircon ages 435 ± 6, 300 ± 4, and 272.5 ± 1.4 (2σ, MSWD = 0.57, N = 5) (Fig. 5 (e′)).

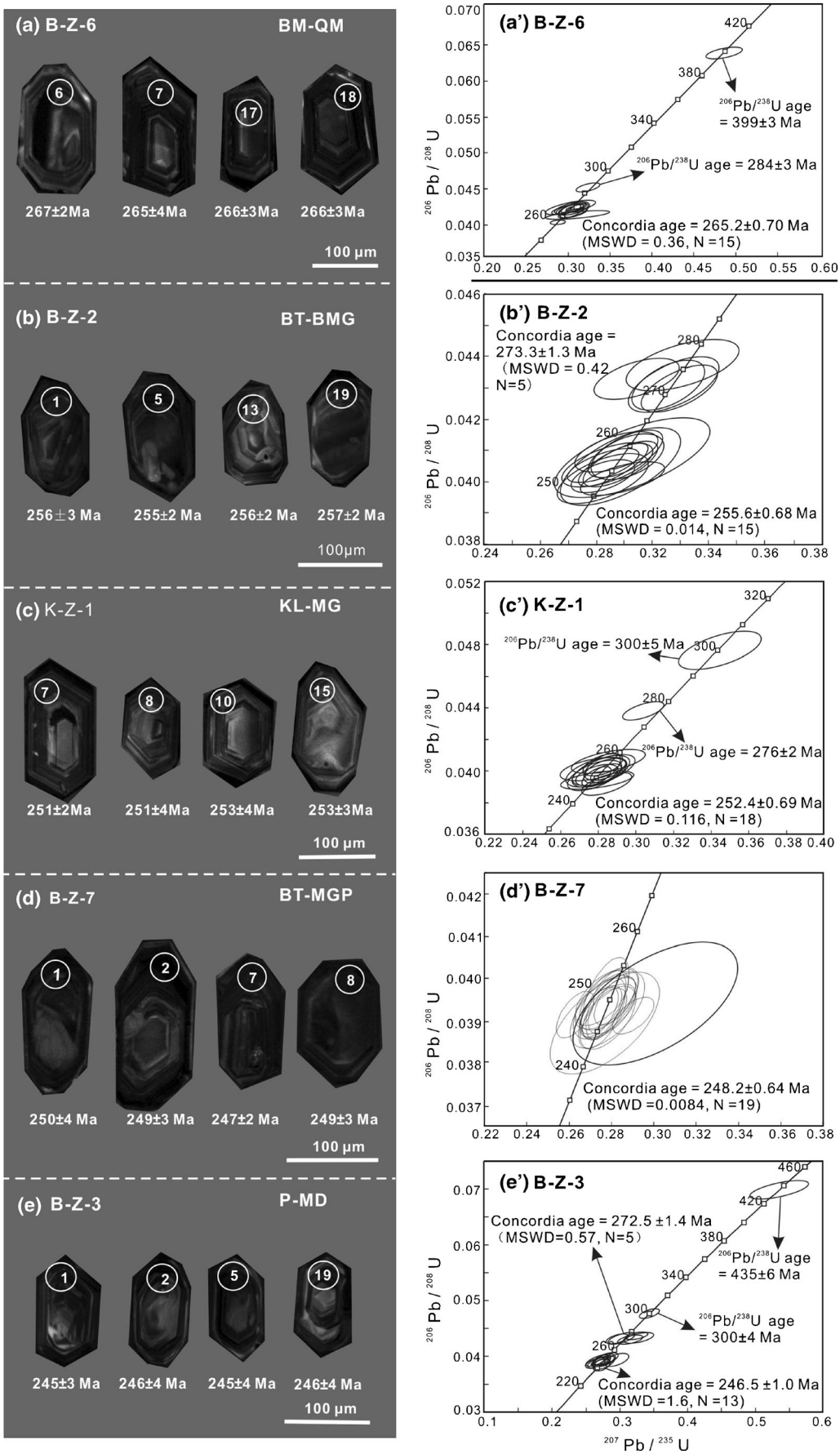
(a) B-Z-6
BM-QM
6
7
17
18
267±2Ma
265±4Ma
266±3Ma
266±3Ma
100 μm
(b) B-Z-2
BT-BMG
1
5
13
19
256±3 Ma
255±2 Ma
256±2 Ma
257±2 Ma
100μm
(c) K-Z-1
KL-MG
7
8
10
15
251±2Ma
251±4Ma
253±4Ma
253±3Ma
100 μm
(d) B-Z-7
BT-MGP
1
2
7
8
250±4 Ma
249±3 Ma
247±2 Ma
249±3 Ma
100 μm
(e) B-Z-3
P-MD
1
2
5
19
245±3 Ma
246±4 Ma
245±4 Ma
246±4 Ma
100 μm
(a') B-Z-6
420
380
340
300
260
206Pb/238U age = 399±3 Ma
206Pb/238U age = 284±3 Ma
Concordia age = 265.2±0.70 Ma
(MSWD = 0.36, N =15)
206 Pb / 208 U
(b') B-Z-2
Concordia age = 273.3±1.3 Ma
(MSWD = 0.42 N=5)
280
270
260
250
Concordia age = 255.6±0.68 Ma
(MSWD = 0.014, N =15)
206 Pb / 208 U
(c') K-Z-1
320
300
280
260
240
206Pb/238U age = 300±5 Ma
206Pb/238U age = 276±2 Ma
Concordia age = 252.4±0.69 Ma
(MSWD = 0.116, N =18)
206 Pb / 208 U
(d') B-Z-7
260
250
240
Concordia age = 248.2±0.64 Ma
(MSWD =0.0084, N =19)
206 Pb / 208 U
(e') B-Z-3
460
420
380
340
300
260
220
Concordia age = 272.5 ±1.4 Ma
(MSWD=0.57, N=5)
206Pb/238U age = 435±6 Ma
206Pb/238U age = 300±4 Ma
Concordia age = 246.5 ±1.0 Ma
(MSWD =1.6, N =13)
206 Pb / 208 U
207 Pb / 235 U

◀ **Fig. 5** Representative cathodoluminescence (CL) images of analyzed zircon grains (*a*–*e*) and corresponding concordia plots of the LA-ICP-MS U–Pb data for zircons (*a′*–*e′*) from intrusions in the Baituyingzi Mo–Cu district, Inner Mongolia. The locations, analytical numbers, and U–Pb ages of the dated grains are also shown. *Errors* are quoted at the 2σ level

Major and trace elements

The major and trace element abundances for 24 samples from the 5 intrusions in the Baituyingzi district are listed in Table S2 and shown in Figs. 6, 7, and 8.

The samples have compositions of 64.43–73.28 wt% SiO_2, 14.0–16.3 wt% Al_2O_3, 1.05–3.27 wt% CaO, 3.29–4.54 wt% K_2O, and 3.14–5.14 wt% Na_2O, with K_2O/Na_2O ratios of 0.64–1.43 and $K_2O + Na_2O$ values of 6.91–9.47 wt%. On a TAS diagram (Fig. 6a), the majority of samples plot in the quartz monzonite and granite fields, which is in accordance with their petrographic names based on the mineral components of the rock specimens. The A/CNK values (molar $Al_2O_3/(CaO + Na_2O + K_2O)$) range from 0.90 to 1.22, and most samples fall between the metaluminous and peraluminous fields and have I-type affinities when plotted on an A/NK versus A/CNK diagram (Fig. 6b). The exceptions are the samples of the ~246 Ma P–MD, which are characterized by peraluminous compositions and plot in the S-type field. These exceptions are probably due to slight alteration as indicated by the relatively high loss-on-ignition (LOI) values. The rocks plot as high-K calc-alkaline or shoshonitic series on the SiO_2 versus K_2O diagram (Fig. 6c), and they lie within the calc-alkalic and alkali-calcic fields of the $Na_2O + K_2O$–CaO versus SiO_2 diagram (Fig. 6d). They also exhibit clearly discernable fractionation trends in the Harker variation diagrams, with most elements decreasing with increasing SiO_2 (except for K_2O; Fig. 7). However, the ~255-Ma BT–MG and the ~248-Ma BT–MGP units are more compositionally variable relative to the other intrusions (Fig. 7), consistent with their wide ranges of mineral compositions (Table 1) and differentiation indices (76.3–88.4 for the ~255 Ma BT–MG and 81.4–91.5 for the ~248 Ma BT–MGP; Table S2).

Chondrite-normalized REE patterns for all samples invariably show enrichment of light rare earth elements (LREEs) and clear depletion of medium to heavy rare earth elements (M-HREEs), with only slightly negative Eu anomalies (Fig. 8a–e). In detail, however, narrow distinctions characterize the different age groups. Overall, the ~248-Ma BT–MGP samples show the steepest REE profiles due to more LREE-enriched and MREE- to HREE-depleted signatures (La_N/Yb_N = 25.6–87.0, La_N/Sm_N = 4.95–8.19, Dy_N/Yb_N = 2.23–5.69), and they have minor to moderate negative Eu anomalies (Eu/Eu^* = 0.58–0.83; Fig. 8d), whereas the samples of the ~252 Ma KL–MG show clearly negative Eu anomalies (Eu/Eu^* = 0.51–0.66) relative to the other intrusions (Fig. 8c). In

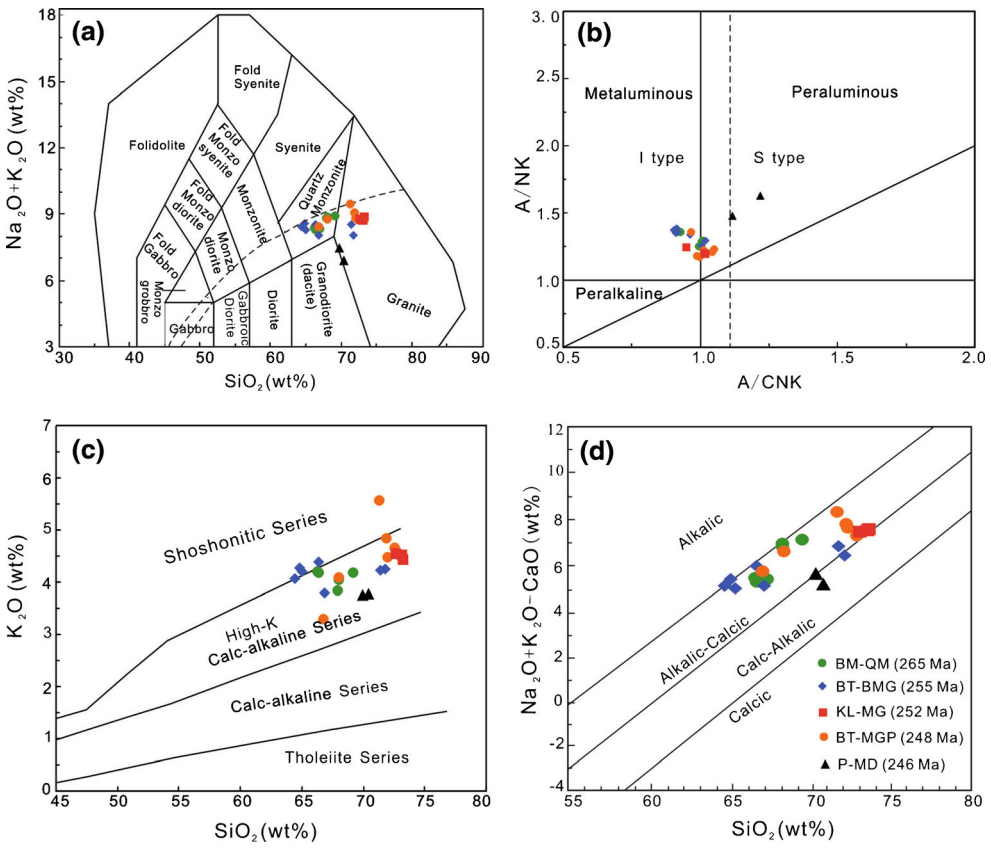

Fig. 6 Plots of **a** $Na_2O + K_2O$ versus SiO_2 (Lebas et al. 1986), **b** A/NK versus A/CNK [A/NK = molar $Al_2O_3/(Na_2O + K_2O)$; A/CNK = molar $Al_2O_3/(CaO + Na_2O + K_2O)$] (Maniar and Piccoli 1989), **c** K_2O versus SiO_2 (Peccerillo and Taylor 1976), and **d** $Na_2O + K_2O$–CaO versus SiO_2 (Frost et al. 2001) for intrusions in the Baituyingzi Mo–Cu district, Inner Mongolia

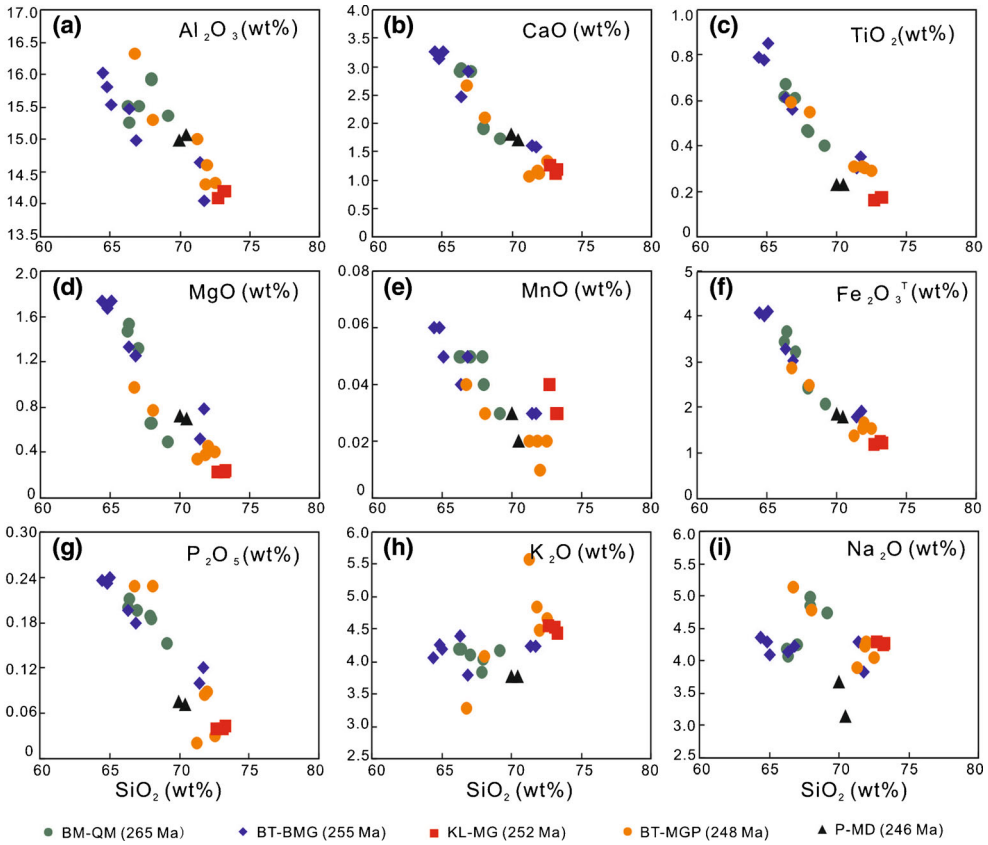

Fig. 7 Harker diagrams showing variations in the major oxides with SiO_2 for intrusions in the Baituyingzi Mo–Cu district, Inner Mongolia

addition, the ~248 Ma BT–MGP and the ~246 Ma P–MD show listric-shaped REE patterns (Fig. 8d, e).

When plotted in spider diagrams normalized to the primitive mantle (Fig. 8a′–e′), all of the samples are characterized by enrichments in large-ion lithophile elements (LILEs; e.g., Rb, K) relative to high-field strength elements (HFSEs; e.g., Nb, Ta), which is typical of subduction-related magmas (Woodhead et al. 1993; Pearce et al. 1999). Moreover, they all show distinct negative anomalies for P and Ti. Negative P anomalies might have resulted from apatite separation. Negative Ti anomalies are considered to be related to fractionation of Ti-bearing phases (ilmenite, titanite, etc.) or indicate that Ti may not have been mobilized from the source and remained in the residuum. In addition, except for the ~246 Ma P–MD, the data show weak negative Ba and positive Th anomalies, which may be related to minor feldspar fractionation.

In the Sr/Y versus Y and $(La/Yb)_N$ versus $(Yb)_N$ diagrams (Fig. 9a, b), the ~265-Ma BM–QM and the ~255-Ma BT–MG rocks straddle the overlapping boundaries of adakite-like rocks and normal arc rocks, with Sr/Y ratios of 29.2–53.6 and La_N/Yb_N ratios of 15.6–39.4. In contrast, the ~252-Ma KL–MG rocks show non-adakitic Sr/Y(11.7–15.6) and La_N/Yb_N (6.01–7.47) ratios and plot in the normal arc field along the plagioclase fractional trend (Fig. 9a, b), which is consistent with the clearly discernible Eu negative anomalies. Compared to the other three intrusions, the ~248-Ma BT–MGP and ~246-Ma P–MD samples have geochemical features similar to adakite, such as high Sr (295–1327 ppm), low Y (5.15–11.4 ppm), and Yb (0.46–1.11 ppm); enrichment of LREEs; and depletion of HREEs, resulting in high Sr/Y (44.9–185) and La_N/Yb_N (25.6–87.0) ratios (Table S2) and plotting consistently within the adakite field along the garnet and amphibole fractional trends (Fig. 9a, b). Taking the listric-shaped REE patterns into account (Fig. 8d, e), the ~248-Ma BT–MGP and the ~246-Ma P–MD rocks probably have evolved along an amphibole fractionation trend (Davidson et al. 2007; Richards 2011b). In addition, the ~248-Ma BT–MGP samples have the largest ranges of Sr/Y and La_N/Yb_N ratios (Fig. 9a, b), also indicating that this unit is compositionally variable.

On the R_1–R_2 and Rb/10–Hf–3Ta tectonic discrimination diagrams (Fig. 10a, b), rock samples from the Baituyingzi complex predominantly straddle the boundary between the volcanic granite and collisional granite fields.

Fig. 8 Chondrite-normalized REE patterns (**a–e**) and primitive mantle-normalized trace element spider diagrams (**a′–e′**) for intrusions in the Baituyingzi Mo–Cu district, Inner Mongolia (normalizing values from Sun and McDonough 1989) ▶

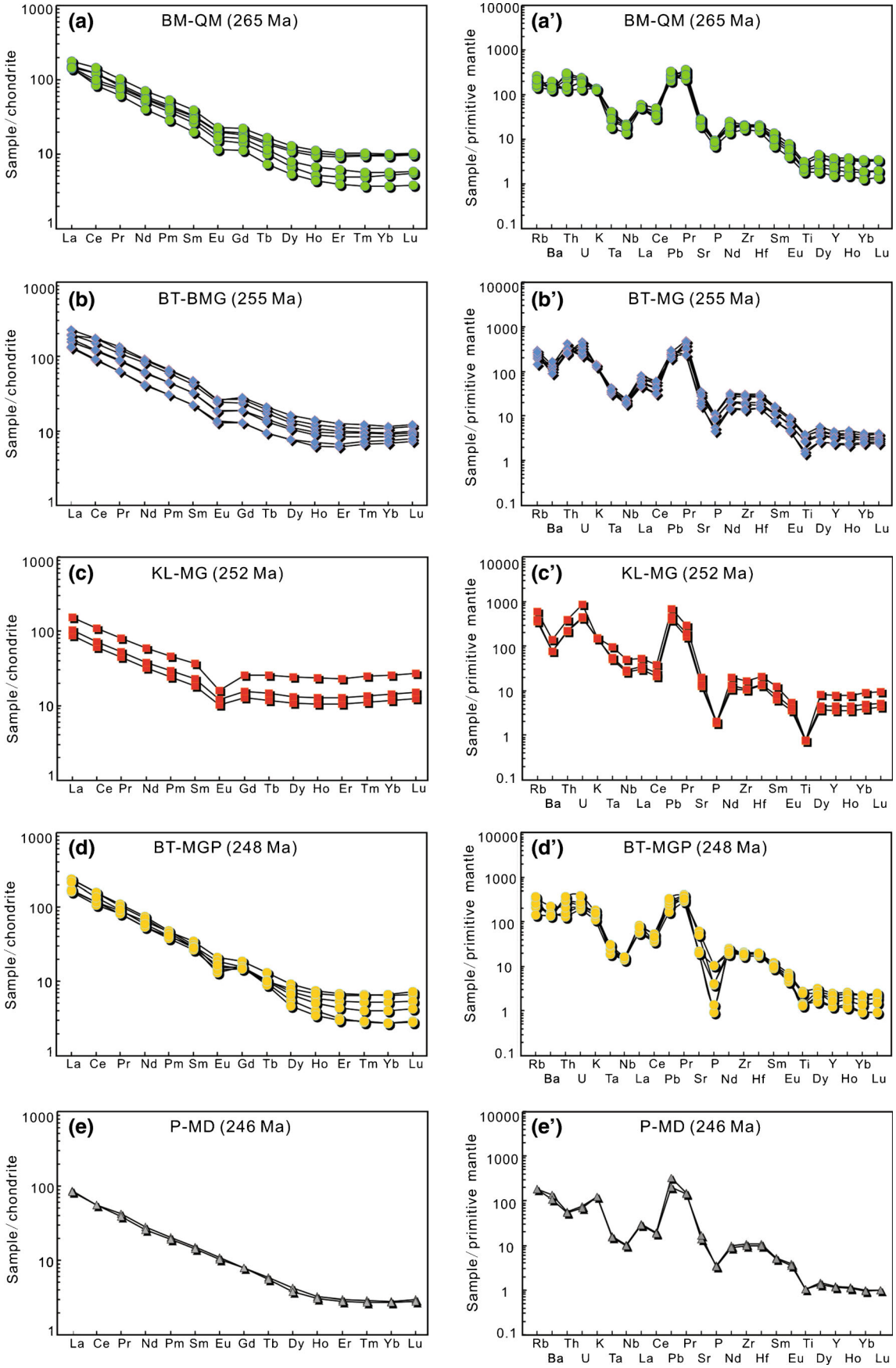
(a)
BM-QM (265 Ma)
(a')
BM-QM (265 Ma)
(b)
BT-BMG (255 Ma)
(b')
BT-MG (255 Ma)
(c)
KL-MG (252 Ma)
(c')
KL-MG (252 Ma)
(d)
BT-MGP (248 Ma)
(d')
BT-MGP (248 Ma)
(e)
P-MD (246 Ma)
(e')
P-MD (246 Ma)
Sample/chondrite
Sample/primitive mantle
La Ce Pr Nd Pm Sm Eu Gd Tb Dy Ho Er Tm Yb Lu
Rb Th K Nb Ce Pr P Zr Sm Ti Y Yb
Ba U Ta La Pb Sr Nd Hf Eu Dy Ho Lu

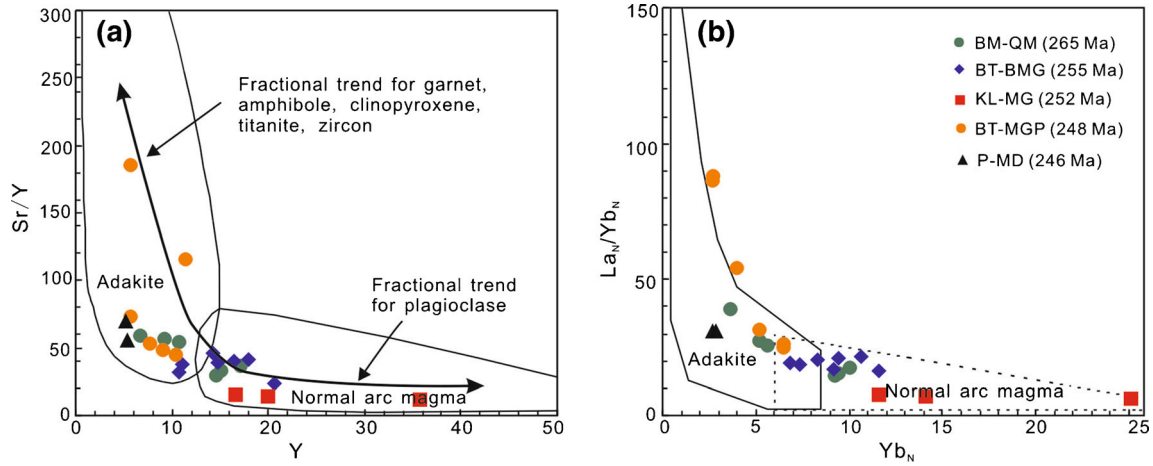

Fig. 9 Plots of **a** $(La/Yb)_N$ versus $(Yb)_N$ (Defant and Drummond 1990) and **b** Sr/Y versus Y (Defant and Drummond 1990) for intrusions in the Baituyingzi Mo–Cu district, Inner Mongolia

Sr–Nd–Pb isotopes

Measured and age-corrected initial Sr–Nd–Pb isotope data are presented in Tables S3 and S4 and are illustrated in Figs. 11 and 12.

The initial $^{87}Sr/^{86}Sr$ ratios of the ~265 Ma BM–QM, the ~255 Ma BT–BMG, ~252 Ma KL–MG, and the ~248 Ma BT–MGP range from 0.70520 to 0.70714. The initial Nd isotopes of these four plutons exhibit some variations between 0.512108 and 0.512371, with the $\varepsilon Nd\ (t)$ ranging from −3.9 to +1.0. Moreover, these four intrusions yield meaningful one-stage Nd model ages (T_{DM}) from 811 to 1183 Ma. In the $\varepsilon Nd\ (t)$ versus $(^{87}Sr/^{86}Sr)_i$ diagram (Fig. 11), these Sr–Nd isotopic values partially overlap with those of the reported igneous rocks adjacent to the Xilamulun fault (Zhou et al. 2001) and the ore-related granites in the Xilamulun Mo metallogenic belt that formed in the Late Jurassic and the Early Cretaceous (e.g., Chen et al. 2008; Qin et al. 2009; Zhang et al. 2009a), which have been demonstrated to show a dominant enriched mantle affinity, supporting a similar origin (derived from a relatively juvenile crustal source).

By comparison, two samples from the ~246 Ma P–MD exhibit distinctively lower initial Nd isotope ratios (0.511558 to 0.511648) and clearly negative $\varepsilon Nd\ (t)$ values (−14.9 to −13.1), although they have initial $^{87}Sr/^{86}Sr$ ratios (0.70515 to 0.70539) similar to those of the other four plutons. The depleted mantle model ages (T_{DM}) for these two samples are 1874 and 2087 Ma, respectively. These Sr–Nd isotopic values of the ~246-Ma P–MD samples are identical to the igneous rocks in the NCC (Zhou et al. 2001) and intrusions in the Chehugou Mo–Cu deposit (Fig. 11; Wan et al. 2009; Zeng et al. 2012), implying that they were likely derived from Paleoproterozoic lower crust or subcontinental lithospheric mantle of the NCC.

Calculated Pb isotopic compositions of samples from the ~265 Ma BM–QM, the ~252 Ma KL–MG, and the ~248 Ma BT–MGP are relatively uniform and slightly

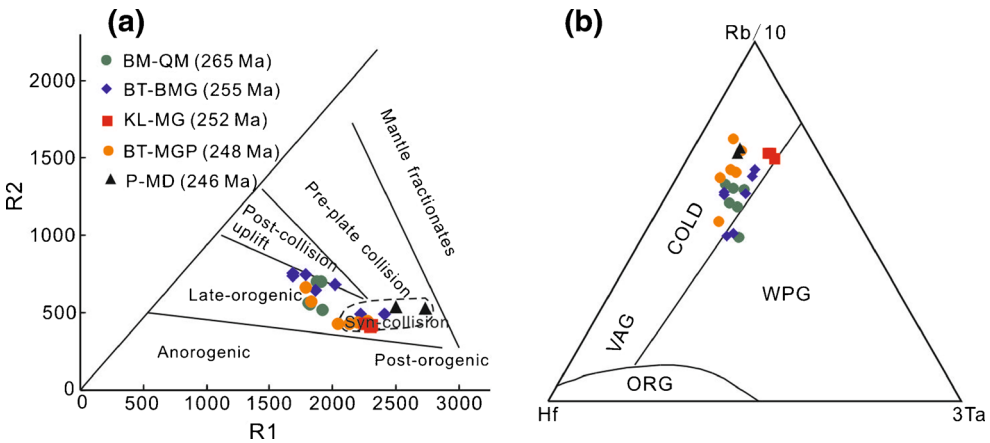

Fig. 10 Tectonic discrimination diagrams for intrusions in the Baituyingzi Mo–Cu district, Inner Mongolia. **a** R_2 versus R_1 (Batchelor and Bowden 1985), where $R_1 = 4Si - 11(Na + K) - 2(Fe + Ti)$ and $R_2 = 6Ca + 2Mg + Al$. **b** Rb/10-Hf-3Ta (Harris et al. 1986). *Syn-COLG* syn-collisional granite, *VAG* volcanic arc granite, *WPG* within-plate granite, *post-COLG* post-collisional granite

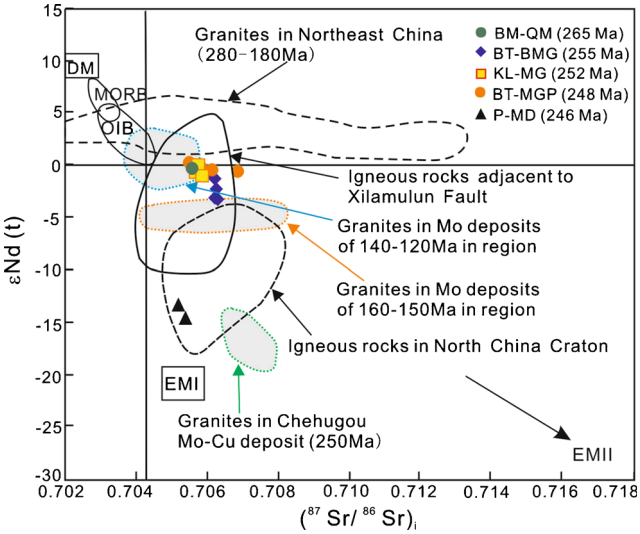

Fig. 11 Initial Sr and Nd isotopic compositions of intrusions in the Baituyingzi Mo–Cu district, Inner Mongolia. Data for granites in northeast China are from Wu et al. (2005, 2011). Data for granites adjacent to the Xilamulun fault and in the North China Craton are from Zhou et al. (2001). Data for the published ore-related granites in the Xilamulun Mo metallogenic belt are from Chen et al. (2008), Qin et al. (2009), Wan et al. (2009), Zhang et al. (2009a), and Zeng et al. (2011, 2012)

radiogenic, with a narrow range of initial $^{206}Pb/^{204}Pb$ (18.137–18.335), $^{207}Pb/^{204}Pb$ (15.591–15.625), and $^{208}Pb/^{204}Pb$ (37.744–38.312) ratios, whereas samples of the ~255 Ma BM–BMG are characterized by a larger range of $^{206}Pb/^{204}Pb$ ratios (17.806 to 18.712). The initial Pb isotope values of these intrusions plot mainly between the orogen and upper crust curves of Zarman and Haines (1988) but close to the orogen curve (Fig. 12a, b). In contrast, the ~246-Ma P–MD samples have comparatively non-radiogenic Pb isotopic signatures ($^{206}Pb/^{204}Pb_t$ = 18.52–18.60, $^{207}Pb/^{204}Pb_t$ = 15.58–15.64, and $^{208}Pb/^{204}Pb_t$ = 38.57–38.80), and they primarily plot near the lower crust curves in the $^{207}Pb/^{204}Pb$ versus $^{206}Pb/^{204}Pb$ (Fig. 12a) and $^{208}Pb/^{204}Pb$ versus $^{206}Pb/^{204}Pb$ diagrams (Fig. 12b).

Discussion

Timing of magmatic and hydrothermal activities

Because only the margin of each zircon grain was selected for analysis to avoid inherited ages, we propose that the youngest zircon U–Pb concordant ages represent the emplacement age of the intrusions, whereas the antecrysts might be inherited from the source region or incorporated during magma ascent. Overall, LA-ICP-MS zircon U–Pb dating results confirm that the intrusions were emplaced between the late Permian and Early Triassic (over a time span of ~20 Ma) as follows: (1) BM–QM (265.2 ± 0.7 Ma), (2) BT–BMG (255.6 ± 0.68 Ma), (3) KL–MG (252.4 ± 0.69 Ma), (4) BT–MGP (248.2 ± 0.64 Ma), and (5) P–MD (246.5 ± 1.0 Ma) (Table 2 and Fig. 5). This order is also consistent with crosscutting relationships (Fig. 3). Additionally, with the exception of the ~248 Ma BT–MGP, xenocrystic zircons of magmatic origin generally occur in the other four intrusions (Table 2), implying the possible existence of early Silurian (435 ± 6 Ma), Early Devonian (399 ± 3 Ma), and late Carboniferous (300 ± 5 Ma) igneous rocks in the Baituyingzi district (although they have not been widely identified), which is consistent with the subduction activity of the Paleo-Asian Ocean (Sengör and Natal'in 1996; Xiao et al. 2003; Kusky et al. 2007; Zhao et al. 2010).

The BT–MGP intrusion is the youngest altered unit and Mo mineralization is centered on it, which suggests that BT–MGP was closely genetically related to the mineralization. Because the ~246 Ma P–MD is fresh and truncates the strongly mineralized BT–MGP (Fig. 3), the zircon LA-ICP-MS U–Pb ages of the BT–MGP and P–MD constrain the age of the Baituyingzi hydrothermal system to between 248.8 ± 1.9 and 246 ± 2.1 Ma in the Early Triassic. This age constraint is broadly consistent with the Mo–Cu mineralization ages (occurring between 245 and 248 Ma) obtained by previous molybdenite Re–Os dating (Sun et al. 2013). The slight difference between ages of magmatic and hydrothermal minerals is considered to be a result of the analytical effects of the various methods on different minerals.

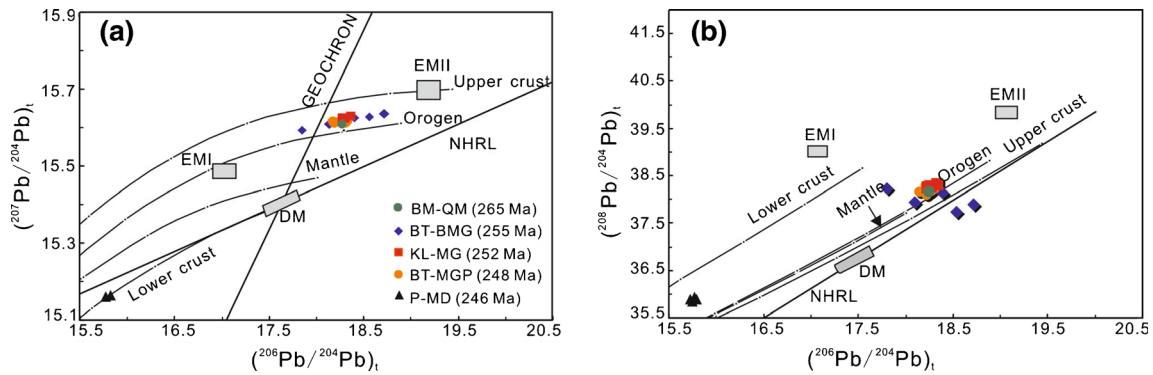

Fig. 12 Initial Pb isotopic compositions of intrusions in the Baituyingzi Mo–Cu district (Zarman and Haines 1988). Data for DM, EMI, and EMII are from Zindler and Hart (1986) and Hofmann (2004)

Table 2 Summary of the zircon U–Pb dating results for intrusions in the Baituyingzi Mo–Cu district, Inner Mongolia

Rock	Occurrence	Mineralization	Sample	Zircon U–Pb dating result (Ma)	
				Crystallization age	Xenocrystic zircon age
Baimashigou quartz monzonite (BM–QM)	Batholith	Barren	B–Z–6	265.2 ± 0.70	284 ± 3, 399 ± 3
Baituyingzi biotite monzogranite (BT–BMG)	Batholith	Mineralization	B–Z–2	255.6 ± 0.68	273.3 ± 1.3
Kulitu monzogranite (KL–MG)	Batholith	Barren	K–Z–1	252.4 ± 0.69	276 ± 2, 300 ± 5
Baituyingzi monzogranite porphyry (BT–MGP)	Stock	Mineralization	B–Z–7	248.2 ± 0.64	None
Post–mineralization dike (P–MD)	Dike	Barren	B–Z–3	246.5 ± 1.0	272.5 ± 1.4, 300 ± 4, 435 ± 6

Tectonic setting

Apart from the Baituyingzi Mo–Cu system, a number of Mo (−Cu) deposits, formed in the late Permian to Middle Triassic (265–235 Ma), have been found in the Xilamulun Mo belt and adjacent areas in recent years (Table 3 and Fig. 1a, b). The tectonic settings for the magmatic event of this stage and the related Mo–Cu mineralization are still ambiguous. Most research has attributed the formation of those deposits to the late extensional stage of the NCC and SC collisional orogeny (e.g., Wan et al. 2009; Zhang et al. 2009a; Duan et al. 2015), whereas Zeng et al. (2012) and Zeng et al. (2013) proposed that the Chehugou Mo–Cu deposit and the Haolibao Mo–Cu deposit may have formed during collision between the NCC and SC.

The tectonic discrimination diagrams (Fig. 10a, b) imply that the Baituyingzi system probably developed in a collisional setting. Moreover, the generation of the Baituyingzi magmatic-hydrothermal system is closely associated with the tectonic evolution of the Paleo-Asian Ocean between the NCC and the SC. Recently, an increasing amount of petrologic, chronological, geotectonic, paleontological, and paleomagnetic evidence has supported the occurrence of the final collision of the NCC and the SC during the early Permian to the Middle Triassic (296–234 Ma) along the Xilamulun Fault (e.g., Xiao et al. 2003, 2009; Li 2006; Wu et al. 2007). Our new ages are coeval with the peak timing of the syn-collisional granitic magmatism in the Xilamulun belt (e.g., Li et al. 2007; Wu et al. 2007). We therefore infer that the late Permian to Early Triassic magmatic and hydrothermal activity in the Baituyingzi district was syn-collisional with respect to the collision between the NCC and SC.

Distinctive features of ore-bearing porphyry

All five intrusions of the Baituyingzi complex are similar in terms of mineral assemblages (Table 1 and Fig. 3) and exhibit clearly discernible fractionation trends in the Harker variation diagrams (Fig. 7). This is consistent with the trace element spider diagrams (Fig. 8a′–e′) and reflects the separation of feldspar, apatite, and possible Ti-bearing phases (e.g., ilmenite, titanite), although they may have remained in the lower crust source. However, the distinct mineralizing potentials of the ore-hosting ~248 Ma BT–MGP and other barren intrusions indicate that there are likely some appreciably different geochemical features between them.

Table 3 Summary of the late Permian to Middle Triassic molybdenum polymetallic ore deposits in the Xilamulun belt and adjacent areas

No.	Deposit	Mineralization type	Metal assemblage	Location	Re–Os isochron age (Ma)	Reference
1	Chaganhua	Porphyry	Mo–Cu	Wulatehou Banner, Bayannaoer League	242.7 ± 3.5	Cai et al. (2011a)
2	Chagande'ersi	Porphyry	Mo–Cu	Wulatehou Banner, Bayannaoer League	243.0 ± 2.2	Cai et al. (2011b)
3	Ulandler	Porphyry	Mo–(Cu)	Sonid Left Banner, Xilin gol League	239.6 ± 3.01	Nie and Jiang (2011)
4	Chehugou	Porphyry-quartz vein	Mo–Cu	Songshan district, Chifeng City	245 ± 5	Zeng et al. (2012)
5	Yuanbaoshan	Quartz vein	Mo	Yuanbaoshan district, Chifeng City	248 ± 3	Liu et al. (2010a)
6	Baimashigou	Quartz vein	Cu–Mo	Aohan Banne, Chifeng City	248.5 ± 6.7	Sun et al. (2013)
7	Baituyingzi	Porphyry	Mo–Cu	Aohan Banne, Chifeng City	248 ± 10	Sun et al. (2013)
8	Kulitu	Quartz vein	Mo–Cu	Aohan Banne, Chifeng City	245 ± 4.3	Sun et al. (2013)
9	Laojiagou	Porphyry	Mo–Cu	Ar Horqin Banner, Chifeng City	234.9 ± 3.1	Duan et al. (2015)
10	Haolibao	Porphyry	Mo–Cu	Ar Horqin Banner, Chifeng City	264.7 ± 2.8	Zeng et al. (2013)

Among the intrusions, the ~248-Ma BT–MGP and ~246-Ma P–MD samples show listric-shaped REE patterns (Fig. 8d, e) and have adakite-like features (e.g., Sr/Y = 44.9–185 and La_N/Yb_N = 25.6–87.0; Table S2 and Fig. 9a, b). Igneous rocks with adakitic affinities (e.g., high Sr/Y ratios) are generally indicative of the presence of residual garnet (or amphibole) and the absence of plagioclase in the source (Defant and Drummond 1990; Condie 2005; Castillo 2006; Macpherson et al. 2006). However, the listric-shaped REE patterns generally further reflect residual amphibole in the source and indicate high water content of magma (e.g., Davidson et al. 2007; Moyen 2009; Richards 2011b; Richards et al. 2012). Therefore, the Sr/Y ratios (Fig. 9a, b) and REE patterns (Fig. 8d, e) probably indicate that both the ~248 Ma BT–MGP and ~246 Ma P–MD are relatively hydrous in the magmatic series. The hydrous features of the ~248 Ma BT–MGP are consistent with the fact that BT–MGP was volatile saturated during evolution (as indicated by UST quartz and pegmatite; Fig. 4g, h′; Harris et al. 2004; Seedorff et al. 2005).

Nevertheless, the 248- and 246-Ma intrusions exhibit geochemical differences. Firstly, the ~248 Ma BT–MGP exhibits a higher degree of fractionation (differentiation indices of 81.4–91.5; Table S2 and Fig. 7) and a steeper REE profile (La_N/Yb_N = 25.6–87.0; Fig. 8d) than those of the ~246 Ma P–MD. Secondly, the ~248-Ma BT–MGP rocks are derived from a relatively juvenile crustal source, whereas the ~246-Ma P–MD samples are likely derived from the Paleoproterozoic lower crust (or subcontinental lithospheric mantle) of the NCC (Figs. 11 and 12).

As suggested by previous studies, (1) high water content is conducive for the generation of a shallow crustal ore-forming magmatic-hydrothermal system (e.g., Richards et al. 2012), (2) a highly differentiated state is necessary for enriching Mo in the magma because Mo is an incompatible element (Candela and Holland 1986; Audétat 2010), and (3) both the juvenile lower crust and the old lower crust (or metasomatized subcontinental lithospheric mantle) are possible sources for Mo (e.g., Pettke et al. 2010; Zhu et al. 2010; Zeng et al. 2014). Our results reveal that a hydrous condition (e.g., high Sr/Y ratios >44 combined with listric-shaped REE patterns) and a highly differentiated condition (e.g., differentiation index > 80 and La_N/Yb_N > 25) may be important chemical indicators for Mo porphyry fertility.

Origins of Mo porphyry fertility

Sr–Nd–Pb results suggest that the five units in Baituyingzi were derived from lower crust (Figs. 11 and 12). The trace element spider diagrams (Fig. 8a′–e′) indicate that the lower crustal magma sources of these intrusions had been once metasomatized by early slab subduction-related fluids or melts (Woodhead et al. 1993; Pearce et al. 1999). Early slab subduction processes could underplate metal- and volatile-rich melts from the slab fluids or melts metasomatized mantle wedge (Rüpke et al. 2004) and generate a fertile metallogenic reservoir (rich in amphibole cumulates) at or near the crust–mantle boundary (Richards 2003, 2009, 2011a; Davidson et al. 2007; Tiepolo and Tribuzio 2008; Pettke et al. 2010). Therefore, the magma sources of the five units should have inherited the arc magma characteristics of abundant water, S, Mo, and Cu and even high oxidation state (Richards 2003, 2009, 2011a; Malaspina et al. 2009).

Trace element ratios, such as Th/Nb, Th/Yb, Ba/Th, and Ba/La, have been used to identify the metasomatic agents and estimate flux from the subducted slab (Pearce and Peate 1995; Johnson and Plank 1999; Class et al. 2000; Kessel et al. 2005; Dokuz 2011). The Ba/Th–Th/Nb (Fig. 13a) and Ba/La–Th/Yb (Fig. 13b) diagrams clearly show that the magma sources of the five intrusions in Baituyingzi were geochemically heterogeneous with the addition of various amounts of slab-derived fluids or melts. Compared to the other three intrusions, the magma sources of the ~248 Ma BT–MGP and ~246 Ma P–MD experienced stronger metasomatism (Fig. 13a, b). Thus, their lower crustal sources should be relatively rich in amphibole cumulates (indicating highly hydrous conditions).

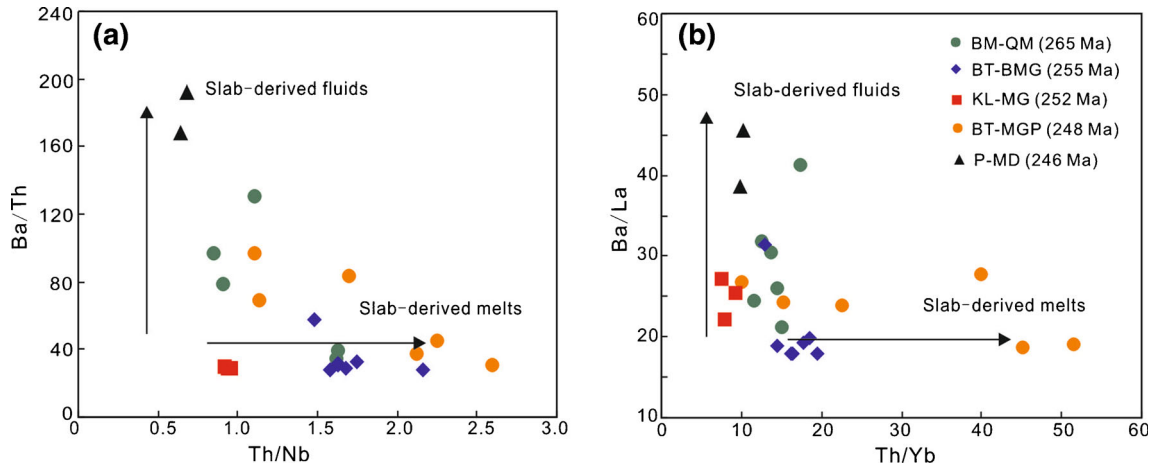

Fig. 13 Plots of **a** Ba/Th versus Th/Nb (Elliott et al. 1997) and **b** Ba/La versus Th/Yb (Dokuz 2011) for intrusions in the Baituyingzi Mo–Cu district, Inner Mongolia

However, the ~246 Ma P–MD shows high Ba/La and Ba/Th ratios (Fig. 13a, b), which indicate that magma sources have been predominantly influenced by slab fluids. In comparison, the ore-forming ~248 Ma BT–MGP had undergone strong metasomatism by slab melt (showing high Th/Nb, Th/Yb ratios; Fig. 13a, b). As suggested by Mungall (2002), the involvement of slab melt enriched in Fe^{3+} during slab subduction could control the redox state of arc magmas above the FMQ buffer. Similar results have also been observed by Liu et al. (2010b) and Wang et al. (2013), who recognized that the involvement of slab melt metasomatism in lower crustal magma sources may significantly promote the oxidation state of the resulting adakitic melts. Thus, the magmatic source of the ~248 Ma BT–MGP may be more oxidized than the ~246 Ma P–MD. Moreover, apart from many porphyry Cu systems (e.g., Liang et al. 2006; Wang et al. 2013; Wang et al. 2014b; Shen et al. 2015), high oxidation states have also been linked with Mo porphyry in the Tongcun Mo deposit, located in northwest Zhejiang, SE China (Qiu et al. 2013).

In summary, the fertility of the ~248 Ma BT–MGP was likely associated with the addition of earlier slab-derived melts to the lower crustal magma source (leading to high water content and possible high oxidation state), whereas the relatively low oxidation state of the magma source (due to metasomatism by slab fluids) probably led to the barren condition of the ~246 Ma P–MD (although the source was also hydrous). In addition, following the suggestion of Richards et al. (2012), we suppose that the formation of the highly differentiated state of the ~248 Ma porphyry can be attributed to the long-lived (~20 Ma) tectonic setting during collision between the NCC and the SC.

Genetic model of the Baituyingzi complex

Combined with the tectonic setting, U–Pb ages, geochemical, and Sr–Nd–Pb isotopic results, we suggest that the complex was generated by partial melting of the juvenile lower crust (containing minor old crustal relicts of the NCC) that was triggered by collision between the NCC and SC during the late Permian to Early Triassic (265 to 246 Ma; Fig. 14b).

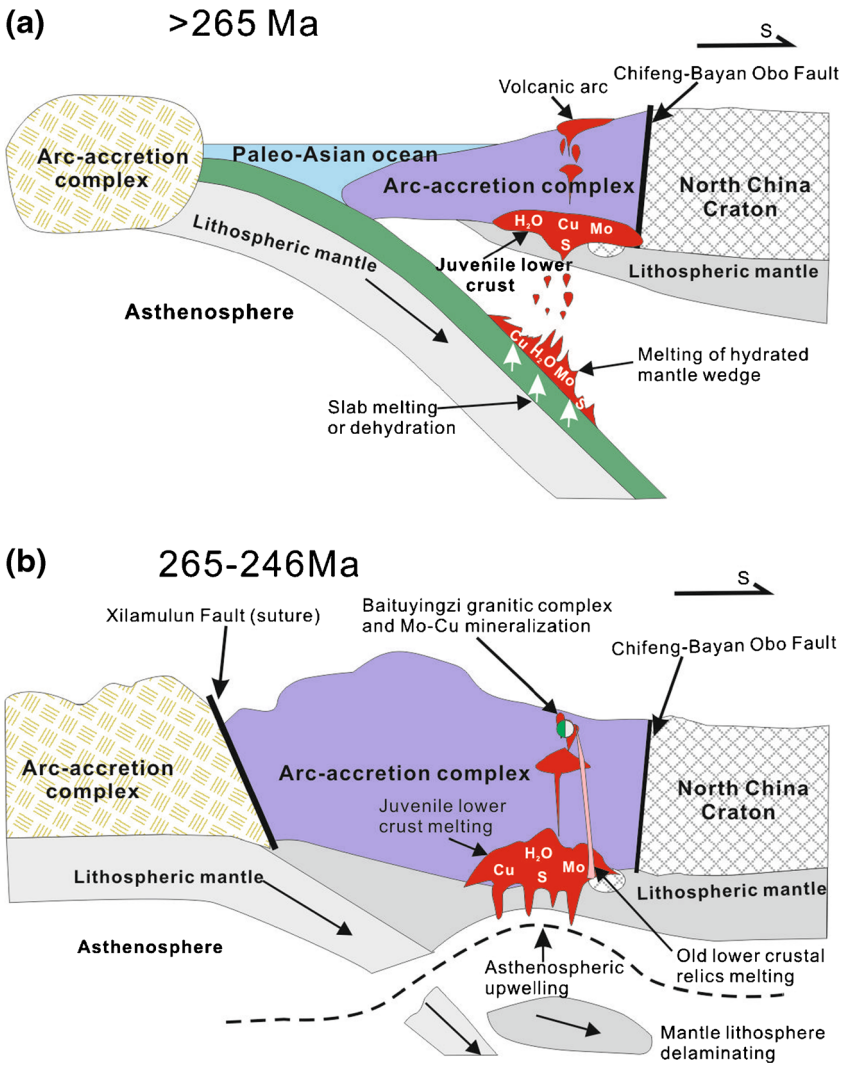

Fig. 14 Sketches showing the genetic model of the Baituyingzi granitic complex, Inner Mongolia. **a** Before ~265 Ma, a series of arc magmas and the mafic lower crust of a juvenile arc formed during subduction of the Paleo-Asian Ocean Plate. The mafic lower crust of the juvenile arc was derived from melting of the fertile mantle wedge metasomatized by various amounts of slab melts or fluids, and it was heterogeneous in terms of water, S, Mo, and Cu contents and possible oxidation state. **b** During 265–246 Ma, collision between the NCC and the SC trigged partial melting of the earlier-formed geochemically heterogeneous juvenile mafic lower crust (containing minor old crustal relicts of NCC) and formed the Baituyingzi granitic complex and the related hydrothermal Mo–Cu system

The lower crust may have been derived from the melting of the fertile mantle wedge metasomatized by various amounts of slab-derived fluids or melts due to earlier subduction events (similar to cases in eastern Turkey (Karsli et al. 2010), southeastern Iran (Shafiei et al. 2009), and south Tibet (Li et al. 2011); Fig. 14a) and was heterogeneous in terms of water, S, Mo, and Cu contents and possible oxidation state. Among the intrusions, the lower crustal magma source of the ~248 Ma BT–MGP was relatively hydrous and possibly oxidized.

The long-time (~20 Ma) collision tectonic setting resulted in establishment of a mature magma-processing (MASH) zone at the base of the crust (Hildreth and Moorbath 1988); the development of relatively long-lived batholithic magma chambers (Richards 2003; Sillitoe 2010); and the generation of early relatively dry and barren intrusions, the later hydrous, differentiated, and possibly oxidized ~248 Ma BT–MGP (and the related hydrothermal Mo–Cu system) and the final hydrous (but barren) ~246 Ma P–MD in the Baituyingzi district.

Conclusions

(1) The Baituyingzi granitic complex was emplaced between the late Permian and Early Triassic (265.2 ± 0.7 to 246.5 ± 1.0 Ma). The Baituyingzi hydrothermal system was related to the Baituyingzi monzogranite porphyry (248.2 ± 0.64 Ma).
(2) The hydrous conditions (e.g., high Sr/Y ratios >44 combined with listric-shaped REE patterns) and highly differentiated conditions (e.g., differentiation index >80 and La_N/Yb_N >25) appear to be important chemical indicators for ~248-Ma porphyry fertility.
(3) The Baituyingzi complex was generated by the partial melting of the juvenile lower crustal magma sources (containing minor old crustal relicts of the NCC) that was triggered by collision between the NCC and SC during the late Permian to Early Triassic.
(4) The magmatic source was derived from the melting of the fertile mantle wedge after various degrees of metasomatism by slab-derived fluids or melts during an earlier subduction event. Thus, the magmatic source was heterogeneous in terms of water, Cu, Mo, and S contents and possible oxidation state.
(5) The fertility of the ~248 Ma porphyry was likely associated with the addition of earlier slab-derived melts to the lower crustal magma source (leading to high water content and possible high oxidation state) and the long-time (~20 Ma) collision tectonic setting in which it formed (resulting in a highly differentiated state).

Acknowledgements This work was financially supported by the National Natural Science Foundation of China (No. 41390443 and No. 41602102) and the Major State Basic Research Program of China (No. 2013 CB429804 and No. 2014 CB440803). Special thanks are extended to Yu-You Gao, Wen-Jun Shen, An-Ming Luo, and Lei Li for their assistance with the field work. We are also grateful to Qi Wang, He Li, Wen-Jun Li, and Lian Zhou for their help with zircon LA-ICP-MS dating, XRF determination, ICP-MS analysis, and Sr–Nd–Pb isotopic measurements, respectively. In addition, two reviewers (Rui Wang and Alan Wainwright), the Associate Editor Thomas Bissig, and the Editor-in-Chief Bernd Lehmann are very much acknowledged for their very thoughtful suggestions and for reviewing the paper several times, which have greatly improved this manuscript. Finally, we are grateful to the editors from the American Journal Experts for checking the language.

Appendix

Zircon LA-ICP-MS U–Pb geochronology analyses

Zircon crystals were extracted by a combination of heavy-liquid and magnetic separation techniques. Individual crystals were then handpicked under a binocular microscope, mounted in epoxy resin, and polished to expose the cores of the grains. Before isotopic analysis, all grains were photographed under transmitted and reflected light and then examined using a CAMECA SX–50 microprobe cathodoluminescence (CL) imaging technique at the Institute of Geology and Geophysics, Chinese Academy of Sciences (IGGCAS), Beijing, China, to identify the internal structures and to ensure a selection of good analytical sites.

Zircon U–Pb dating was conducted by LA-ICP-MS at the State Key Laboratory of Geological Processes and Mineral Resources (GPMR), China University of Geosciences, Wuhan. The analyses were obtained using a laser-ablation microprobe coupled with an Agilent 7500a ICP-MS. Detailed analytical procedures were described by Liu et al. (2008, 2010c). Because inherited zircons usually form cores to new zircons crystallized from the magma, only the margin of each zircon grain was selected for analyzing. The spot size averaged approximately 30 μm, and each analysis incorporated a background acquisition of approximately 20–30 s (gas blank) followed by 50-s data acquisition from the sample, employing line scans rather than spot analyses in order to minimize within-run elemental fractionation (Tafti et al. 2009). NIST 612 glass was used as an internal standard for U, Th, and Pb analyses, and zircon 91,500 (Wiedenbeck et al. 1995) was used as the external calibration standard for U–Pb dating. Common Pb was corrected according to the method proposed by Andersen (2002). Off-line isotopic ratios and element concentrations were calculated using ICPMSDataCal software (Liu et al. 2010c). Age calculations and concordia diagrams were generated using ISOPLOT (version 3.0) (Ludwig 2003). The uncertainties for individual analyses (ratios and ages) are quoted at the 1σ level, whereas the errors on concordia and mean ages are quoted at the 2σ level.

Major and trace element geochemical analyses

The samples were crushed to 200 mesh using an agate mill after removal of weathered surfaces. Whole-rock geochemical analyses were performed at IGGCAS.

Major elements were determined by XRF–1500 Sequential X-ray Fluorescence Spectrometry of fused glass beads, of which the FeO concentration was analyzed using a conventional titration procedure. The accuracy and reproducibility were monitored by Chinese national standard sample GSR1, with a relative standard deviation of better than 1%. Analytical precisions for major elements are generally within 5%.

Trace elements (including REE) were determined with a FELEMENT ICP-MS. Approximately 50 mg of powder for each sample was dissolved in Savillex Teflon® beakers with a HF–HNO_3 mixture for 4 days at approximately 200 °C, dried, and then digested with HNO_3 at 150 °C for 1 day. Dissolved samples were diluted to 50 ml with 1% HNO_3 for ICP-MS analysis. Indium was used as an internal standard for correction of matrix effects and instrument drift. Standard samples GRS1 were used to monitor the analytical error and drift with a periodicity of 10%, and the relative standard deviation is better than 3%. Analyzed uncertainties of ICP-MS data at the ppm level are better than ±3% to ±10% for trace elements and ±5% to ±10% for REE.

Sr–Nd–Pb isotopic analyses

Sr–Nd–Pb isotopes were performed on a Finnigan MAT-262 mass spectrometer at the GPMR. Detailed chemical separation and isotopic measurement procedures are similar to those described by Wu et al. (2005). Analytical errors are given as 2σ.

For Rb–Sr and Sm–Nd isotope analyses, 100 mg of powder (200 mesh) of each sample was spiked with mixed isotope tracers (^{87}R-^{84}Sr, ^{149}Sm-^{150}Nd) and digested in Teflon capsules with a mixture of distilled HF + HNO_3 + $HClO_4$ acids. Digested samples were dried and redissolved in HBr + HCl and then dried again and redissolved in 0.5 N HCl to extract Sr and Nd. The following separation and purification of Sr and REE were realized in cation exchange columns with 2 ml of AG50 W–X12 (200–400-mesh resin), whereas Sm and Nd were separated and purified through a quartz ion-exchange column filled with 1 ml of P507 levextrel resin. The mass fractionation corrections of $^{87}Sr/^{86}Sr$ and $^{143}Nd/^{144}Nd$ isotopic ratios were based on $^{86}Sr/^{88}Sr = 0.1194$ and $^{146}Nd/^{144}Nd = 0.7219$, respectively. Analyses of Sr standard solution (National Bureau of Standards (NBS) 987) yielded an $^{87}Sr/^{86}Sr$ ratio of 0.710244 ± 4 (2σ), whereas the Nd standard solution (BCR–1) yielded a $^{143}Nd/^{144}Nd$ ratio of 0.512633 ± 7 (2σ) during data acquisition. Total procedural blanks were 50 to 100 pg for Sr and 100 to 300 pg for Nd, and the estimated analytical uncertainties of $^{87}Rb/^{86}Sr$ and $^{147}Sm/^{144}Nd$ ratios were less than 0.5%.

For Pb isotope analyses, approximately 100 mg of powder was dissolved in Teflon beakers with a HF + HNO_3 mixture. After drying, the digested samples were redissolved in HBr + HCl mixture for Pb separation. Then, the extracted Pb was purified in a second column with 150 μm of AG1X8 anionic resin. A factor of 1‰ per mass unit for instrumental mass fractionation was applied to the Pb analyses, using NBS 981 as reference material. The NBS 981 standard yielded $^{206}Pb/^{204}Pb = 16.916 \pm 0.009$ (2σ), $^{207}Pb/^{204}Pb = 15.461 \pm 0.010$ (2σ), and $^{208}Pb/^{204}Pb = 36.616 \pm 0.012$ (2σ), with uncertainties of <0.1% at the 95% confidence level. Total procedural blanks for Pb were less than 200 pg.

References

Audétat A, Pettke T (2006) Evolution of a porphyry–Cu mineralized magma system at Santa Rita, New Mexico (USA). J Petrol 47: 2021–2046

Audétat A (2010) Source and evolution of molybdenum in the porphyry Mo (−Nb) deposit at cave peak, Texas. J Petrol 51:1739–1760

Andersen T (2002) Correction of common lead in U–Pb analyses that do not report 204 Pb. Chem Geol 192:59–79

Ballard JR, Palin JM, Campbell IH (2002) Relative oxidation states of magmas inferred from Ce(IV)/Ce(III) in zircon: application to porphyry copper deposits of northern Chile. Contrib Mineral Petrol 144:347–364

Batchelor RA, Bowden P (1985) Petrogentic interpretation of granitoid rocks series using multicationic parameters. Chem Geol 48:43–55

Cai MH, Zhang ZG, Qu WJ, Peng ZA, Zhang SQ, Xu M, Chen Y, Wang XB (2011a) Geological characteristics and Re–Os dating of the Chaganhua molybdenum deposit in Urad rear banner, western Inner Mongolia. Acta Geosci Sin 32:64–68 In Chinese with English abstract

Cai MH, Peng ZA, Qu WJ, He ZY, Feng G, Zhang SQ, Xu M, Chen Y (2011b) Geological characteristics and Re–Os dating of molybdenites in Chagandeersi molybdenum deposit, western Inner Mongolia. Mineral Deposits 30:377–384 In Chinese with English abstract

Candela PA, Holland HD (1986) A mass transfer model for copper and molybdenum in magmatic hydrothermal systems: the origin of porphyry-type ore deposits. Econ Geol 81:1–19

Carten RB, White WH, Stein HJ (1993) High-grade granite-related molybdenum systems: classification and origin. In: Kirkham RV, Sinclair WD, Thorpe RI, Duke JM (eds) Mineral Deposit Modeling, Geological Association of Canada, Special Papers, vol 40, pp. 521–554

Castillo PR (2006) An overview of adakite petrogenesis. Chin Sci Bull 51:617–627

Chambefort I, Dilles JH, Kent AJR (2008) Anhydrite-bearing andesite and dacite as a source for sulfur in magmatic-hydrothermal mineral deposits. Geology 36:719–722

Chen ZG, Zhang LC, Wu HY, Wan B, Zeng QD (2008) Geochemistry study and tectonic background of a style host granite in Nianzigou Mo deposit in Xilamulun Mo metallogenic belt, Inner Mongolia. Acta Petrologica Sinca 24:879–889 In Chinese with English abstract

Condie KC (2005) TTGs and adakites: are they both slab melts? Lithos 80:33–44

Class C, Miller DM, Goldstein SL, Langmuir CH (2000) Distinguishing melt and fluid subduction components in Umnak Volcanics, Aleutian Arc. G3 1: 1004

Davidson JP, Turner S, Handley H, Macpherson C, Dosseto A (2007) Amphibole "sponge" in arc crust? Geology 35:787–790

Davis GA, Xu B, Zheng YD, Zhang WJ (2004) Indosinian extension in the Solonker suture zone: the Sonid Zuoqi metamorphic core complex, Inner Mongolia, China. Earth Sci Front 11:135–144

Defant MJ, Drummond MS (1990) Derivation of some modern arc magmas by melting of young subducted lithosphere. Nature 347: 662–665

Dokuz A (2011) A slab detachment and delamination model for the generation of carboniferous high-potassium I-type magmatism in the eastern Pontides, NE Turkey: the Kose composite pluton. Gondwana Res 19:926–944

Duan XX, Zeng QD, Yang YH, Liu JM, Chu SX, Sun Y, Zhang ZL (2015) Triassic magmatism and Mo mineralization in northeast China: geochronological and isotopic constraints from the Laojiagou porphyry Mo deposit. Int Geol Rev 57:55–75

Elliott T, Plank T, Zindler A, White W, Bourdon B (1997) Element transport from slab to volcanic front at the Mariana arc. J Geophys Res 102:14991–15019

Fernando C, John MH, Paul WOH, Peter K (2003) Atlas of zircon textures. Rev Mineral Geochem 53:469–500

Frost BR, Barnes CG, Collins WJ, Arculus RJ, Ellis DJ, Frost CD (2001) A geochemical classification for granitic rocks. J Petrol 42:2033–2048

Hattori KH, Keith JD (2001) Contribution of mafic melt to porphyry copper mineralization: evidence from Mount Pinatubo, Philippines, and Bingham Canyon, Utah, U.S.A. Mineral Deposita 36:799–806

Harris AC, Kamenetsky VS, White NC, Steele DA (2004) Volatile phase separation in silicic magmas at Bajo de la Alumbrera porphyry Cu-Au deposit, NW Argentina. Resourse Geol 54:341–356

Harris NBW, Pearce JA, Tindle AG (1986) Geochemical characteristics of collision-zone magmatism. In: Coword MP, Reis AC (eds) Collision tactonics, vol 19. Special Publication Geological Society, London, pp. 67–81

Hildreth W, Moorbath S (1988) Crustal contributions to arc magmatism in the Andes of central Chile. Contrib Mineral Petrol 98:455–489

Hofmann AW (2004) Sampling mantle heterogeneity through oceanic basalts: isotopes and trace elements. Treatise Geochem 2:61–103

Hou ZQ, Pan XF, Li QY, Yang ZM, Song YC (2013) The giant Dexing porphyry Cu–Mo–Au deposit in East China: product of melting of juvenile lower crust in an intracontinental setting. Mineral Deposita 48:1019–1045

Jahn BM, Wu FY, Chen B (2000) Granitoids of the central Asian orogenic belt and continental growth in the Phanerozoic. Transactions of the Royal Society of Edinburgh. Earth Sci 91:181–193

Jahn BM, Windley B, Natal'in B, Dobretsov N (2004) Phanerozoic continental growth in central Asia. J Asian Earth Sci 23:599–603

Jian P, Liu DY, Kröner A, Windley BF, Shi YR, Zhang FQ, Shi G, Miao L, Zhang W, Zhang JS, Zhang L, Ren J (2008) Time scale of an early to mid-Paleozoic orogenic cycle of the long-lived central Asian Orogenic Belt, Inner Mongolia of China: implications for continental growth. Lithos 101:233–259

Jian P, Liu DY, Kröner A, Windley BF, Shi YR, Zhang W, Zhang FQ, Miao LC, Zhang LQ, Tomurhuu D (2010) Evolution of a Permian intraoceanic arc-trench system in the Solonker suture zone, central Asian Orogenic Belt, China and Mongolia. Lithos 118:169–190

Johnson MC, Plank T (1999) Dehydration and melting experiments constrain the fate of subducted sediments. G3 1: 1007–1026

Karsli O, Dokuz A, Uysal I, Aydin F, Kandemir R, Wijbrans J (2010) Generation of the early Cenozoic adakitic volcanism by partial melting of mafic lower crust, eastern Turkey: implications for crustal thickening to delamination. Lithos 114:109–120

Kessel R, Schmidt MW, Ulmer P, Pettke T (2005) Trace element signature of subduction-zone fluids, melts and supercritical liquids at 120–180 km depth. Nature 437:724–727

Kusky TM, Windley BF, Zhai MG (2007) Tectonic evolution of the North China block: from orogen to craton to orogen. In: Zhai MG, Windley BF, Kusky TM, Meng QR (eds) Mesozoic subcontinental lithospheric thinning under eastern Asia. Geological Society, London, pp. 1–34

Lebas MJ, Lemaitre RW, Streckeisen A, Zanettin B (1986) A chemical classification of volcanic-rocks based on the total alkali silica diagram. J Petrol 27:745–750

Lerchbaumer L, Audétat A (2013) The metal content of silicate melts and aqueous fluids in subeconomically Mo mineralized granites: implications for porphyry Mo genesis. Econ Geol 108:987–1013

Li JX, Qin KZ, Li GM, Xiao B, Chen L, Zhao JX (2011) Post-collisional ore-bearing adakitic porphyries from Gangdese porphyry copper belt, southern Tibet: melting of thickened juvenile arc lower crust from Gangdese porphyry copper belt, southern Tibet: melting of thickened juvenile arc lower crust. Lithos 126:265–277

Li JY (2006) Permian geodynamic setting of northeast China and adjacent regions: closure of the paleo-Asian Ocean and subduction of the paleo-Pacific plate. J Asian Earth Sci 26:207–224

Li JY, Gao LM, Sun GH, Li YP, Wang YB (2007) Shuangjingzi middle Triassic syn-collisional crust-derived granite in the East Inner Mongolia and its constraint on the timing of collision between Siberian and Sino-Korean paleo-plates. Acta Petrol Sin 23:565–582 In Chinese with English abstract

Li S, Wang T, Wilde SA, Tong Y, Hong DW, Guo QQ (2012) Geochronology, petrogenesis and tectonic implications of Triassic granitoids from Beishan, NW China. Lithos 134–135:123–145

Liang HY, Campbell IH, Allen C, Sun WD, Liu CQ, Yu HX, Xie YW, Zhang YQ (2006) Zircon Ce^{4+}/Ce^{3+} ratios and ages for Yulong ore-bearing porphyries in eastern Tibet. Mineral Deposita 41:152–159

Liu W, Siebel W, Li XJ, Pan XF (2005) Petrogenesis of the Linxi granitoids, northern Inner Mongolia of China: constraints on basaltic underplating. Chem Geol 219:5–35

Liu JM, Zhao Y, Sun YL, Li DP, Liu J, Chen BL, Zhang SH, Sun WD (2010a) Recognition of the latest Permian to early Triassic Cu–Mo mineralization on the northern margin of the North China block and its geological significance. Gondwana Res 17:125–134

Liu SA, Li S, He Y, Huang F (2010b) Geochemical contrasts between early cretaceous ore-bearing and ore-barren high-Mg adakites in central-eastern China: implications for petrogenesis and Cu–Au mineralization. Geochim Cosmochim Acta 74:7160–7178

Liu YS, Hu ZC, Gao S, Günther D, Xu J, Gao CG, Chen HH (2008) In situ analysis of major and trace elements of anhydrous minerals by LA-ICP-MS without applying an internal standard. Chem Geol 257: 34–43

Liu YS, Gao S, Hu ZC, Gao CG, Zong KQ, Wang DB (2010c) Continental and oceanic crust recycling-induced melt-peridotite interactions in the trans-North China orogen: U–Pb dating, Hf isotopes and trace elements in zircons of mantle xenoliths. J Petrol 51:537–571

Ludwig KR (2003) ISOPLOT 3.00: a geochronological toolkit for Microsoft excel. Berkeley Geochronology Center, Berkeley: California

Macpherson CG, Dreher ST, Thirlwall MF (2006) Adakites without slab melting: high pressure differentiation of island arc magma, Mindanao, the Philippines. Earth Planet Sci Lett 243:581–593

Malaspina N, Poli S, Fumagalli P (2009) The oxidation state of metasomatized mantle wedge: insights from C–O–H-bearing garnet peridotite. J Petrol 50:1533–1552

Maniar PD, Piccoli PM (1989) Tectonic discrimination of granitoids. Geol Soc Am Bull 101:635–643

Mao JW, Xie GQ, Zhang ZH, Li XF, Wang YT, Zhang CQ, Li YF (2005) Mesozoic large-scale metallogenic pulses in North China and corresponding geodynamic settings. Acta Petrol Sin 21:169–188 In Chinese with English abstract

Mao JW, Pirajno F, Lehmann B, Luo MC, Berzina A (2014) Distribution of porphyry deposits in the Eurasian continent and their corresponding tectonic settings. J Asian Earth Sci 79:576–584

Moyen JF (2009) High Sr/Y and La/Yb ratios: the meaning of the "adakitic signature". Lithos 112:556–574

Mungall JE (2002) Roasting the mantle: slab melting and the genesis of major Au and Au-rich Cu deposits. Geology 30:915–918

Nie FJ, Jiang SH (2011) Geological setting and origin of Mo–W–Cu deposits in the Honggor–Shamai District, vol 61. North China: Resource Geology, Inner Mongolia, pp. 344–355

Pearce JA, Peate DW (1995) Tectonic implications of the composition of volcanic arc magmas. Earth Planet Sci Lett 23:251–286

Pearce JA, Kempton PD, Nowell GM, Noble SR (1999) Hf–Nd element and isotope perspective on the nature and provenance of mantle and subduction components in western Pacific arc-basin systems. J Petrol 40:1579–1611

Peccerillo A, Taylor SR (1976) Geochemistry of Eocene calc-alkaline volcanic rocks from the Kastamonu area, northern Turkey. Contrib Mineral Petrol 58:63–81

Pettke T, Oberli F, Heinrich CA (2010) The magma and metal source of giant porphyry-type ore deposits, based on lead isotope microanalysis of individual fluid inclusions. Earth Planet Sci Lett 296:267–277

Qin F, Liu JM, Zeng QD, Luo ZH (2009) Petrogenetic and metallogenic machenism of the Xiaodonggou porphyry molybdenum deposit in Hexigten banner, Inner Mongolia. Acta Petrol Sin 25:3357–3368 In Chinese with English abstract

Qin KZ, Li GM, Zhao JX, Li JX, Xue GQ, Yan G, Su DK, Xiao B, Chen L, Fan X (2008) Discovery of Sharang large-scale porphyry molybdenum deposit, the first single Mo deposit in Tibet and its significance. Geol China 35:1101–1112 In Chinese with English abstract

Qiu JT, Yu XQ, Santosh M, Zhang DH, Chen SQ, Li PJ (2013) Geochronology and magmatic oxygen fugacity of the Tongcun molybdenum deposit, northwest Zhejiang, SE China. Mineral Deposita 48:585–602

Richards JP (2003) Tectono-magmatic precursors for porphyry Cu–(Mo–Au) deposit formation. Econ Geol 98:1515–1533

Richards JP (2009) Postsubduction porphyry Cu-Au and epithermal Au deposits: products of remelting of subduction-modified lithosphere. Geology 37:247–225

Richards JP (2011a) Magmatic to hydrothermal metal fluxes in convergent and collided margins. Ore Geol Rev 40:1–26

Richards JP (2011b) High Sr/Y are magmas and porphyry Cu ± Mo ± Au deposits: just add water. Econ Geol 106:1075–1081

Richards JP, Spell S, Rameh E, Razique A, Fletcher T (2012) High Sr/Y magmas reflect arc maturity, high magmatic water content, and porphyry Cu ± Mo ± Au potential: examples from the Tethyan arcs of central and eastern Iran and western Pakistan. Econ Geol 107:295–332

Rüpke LH, Morgan JP, Hort M, Connolly JAD (2004) Serpentine and the subduction zone water cycle. Earth Planet Sci Lett 223:17–34

Samuel AB, Mark DS (2003) High-precision U–Pb zircon geochronology and the stratigraphic record. Rev Mineral Geochem 53:305–326

Seedorff E, Dilles JH, Proffett JM, Einaudi MT, Zurcher L, Stavast WJA, Johnson DA, Barton MD (2005) Porphyry deposits: characteristics and origin of hypogene features. Econ Geol 100:251–298

Seltmann RT, Porter M, Pirajno F (2014) Geodynamics and metallogeny of the central Eurasian porphyry and related epithermal mineral systems: a review. J Asian Earth Sci 79:810–841

Sengör AMC, Natal'in BA (1996) Paleotectonics of Asia: fragments of a synthesis. The tectonic evolution of Asia. Cambridge University Press, Cambridge, pp. 486–640

Shafiei B, Haschke M, Shahabpour J (2009) Recycling of orogenic arc crust triggers porphyry Cu mineralization in Kerman Cenozoic arc rocks, southeastern Iran. Mineral Deposita 44:265–283

Shen P, Hattori K, Pan HD, Jackson S, Seitmuratova E (2015) Oxidation condition and metal fertility of granitic magmas: zircon trace-element data from porphyry Cu deposits in the central Asian Orogenic Belt. Econ Geol 110:1861–1878

Sillitoe RH (2010) Porphyry copper systems. Econ Geol 105:3–41

Simmons TA, Tosdal RM, Wooden JL, Mattos R, Concha O, Mccracken S, Beale T (2013) Punctuated magmatism associated with porphyry Cu-Mo formation in the Paleocene to Eocene of southern Peru. Econ Geol 108:625–639

Sinclair WD (2007) Porphyry deposits. In: Goodfellow WD (eds) Mineral deposits of Canada: a synthesis of major deposit-types, district metallogeny, the evolution of geological provinces, and exploration methods. Geological Association of Canada, Newfoundland, Canada. Mineral Deposits Division, Special Publication 5:223–243

Stavast WJA, Keith JD, Christiansen EH, Dorais MJ, Tingey D, Larocque A, Evans N (2006) The fate of magmatic sulfides during intrusion or eruption, Bingham and Tintic districts, Utah. Econ Geol 101:329–345

Steve L, Plumlee GS (2009) Climax-type porphyry molybdenum deposits. U.S. Geological Survey Open-File Report 2009–1215: 16

Sun Y, Liu JM, Zeng QD (2012) An approach to the metallogenic mechanism of porphyry copper (molybdenum) deposits and porphyry molybdenum (copper) deposits: influence of evolving processes of ore-forming fluids and tectonic settings. Earth Science Frontiers 19: 36–50 In Chinese with English abstract

Sun Y, Liu JM, Zeng QD, Chu XS, Zhou LL, Wu GB, Gao YY, Shen WJ (2013) Geological characteristics and molybdenite Re-Os ages of the Baituyingzi Mo–Cu field, eastern Inner Mongolia and their geological implications. Acta Petrol Sin 29:241–254 In Chinese with English abstract

Sun SS, McDonough W (1989) Chemical and isotopic systematics of oceanic basalts: implications for mantle composition and processes. In: Saunders AD, Norry MJ (eds) Magmatism in the ocean basins, Geological Society Special Publication, vol 42, pp. 313–345

Tafti R, Mortensen JM, Lang JR, Rebagliati M, Oliver JL (2009) Jurassic U-Pb and Re–Os ages for newly discovered Xietongmen Cu–Au porphyry district, Tibet: implications for metallogenic epochs in the southern Gangdese Belt. Econ Geol 104:127–136

Tiepolo M, Tribuzio R (2008) Petrology and U–Pb zircon geochronology of amphibole-rich cumulates with sanukitic affinity from husky ridge (northern Victoria land, Antarctica): insights into the role of amphibole in the petrogenesis of subduction-related magmas. J Petrol 49:937–970

Wan B, Ernst H, Zhang LC, Alexander R, Chen ZG, Wu HY, Chen FK (2009) Rb-Sr geochronology of chalcopyrite from the Chehugou porphyry Mo–Cu deposit (northeast China) and geochemical constraints on the origin of hosting granites. Econ Geol 104:351–363

Wang FY, Liu SA, Li SG, He YS (2013) Contrasting zircon Hf-O isotopes and trace elements between ore-bearing and ore-barren adakitic rocks in central-eastern China: implications for genetic relation to Cu-Au mineralization. Lithos 156–159:97–111

Wang R, Richards JP, Hou ZQ, Yang ZM, Dufrane SA (2014a) Increased magmatic water content—the key to Oligo-Miocene porphyry Cu-Mo ± Au formation in the eastern Gangdese Belt, Tibet. Econ Geol 109:1315–1339

Wang R, Richards JP, Hou ZQ, Yang ZM, Gu ZB, Dufrane SA (2014b) Increasing magmatic oxidation state from Paleocene to Miocene in the eastern Gangdese Belt, Tibet: implication for collision-related porphyry Cu-Mo +/− Au mineralization. Econ Geol 109:1943–1965

Westra G, Keith SB (1981) Classification and genesis of stockwork molybdenum deposits. Econ Geol 76:844–887

Wiedenbeck M, Alle P, Corfu F, Griffin WL, Meier M, Oberli F, Quadt AV, Roddick JC, Spiegel W (1995) Three natural zircon standards for U–Th–Pb, Lu-Hf, trace element and REE analyses. Geostand Geoanalytical Res 19:1–23

Windley BF, Alexeiev D, Xiao WJ, Kroner A, Badarch G (2007) Tectonic models for accretion of the central Asian orogenic belt. J Geol Soc, London 164:31–47

Woodhead J, Eggins S, Gamble J (1993) High field strength and transition element systematics in island and back-arc basin basalts: evidence for multi-phase extraction and a depleted mantle wedge. Earth Planet Sci Lett 114:491–504

Wu FY, Sun DY, Li HM, Jahn BM, Wilde SA (2002) A-type granites in northeastern China: age and geochemical constraints on their petrogenesis. Chem Geol 187:143–173

Wu FY, Zhao GC, Wilde SA, Sun DY (2005) Nd isotopic constraints on crustal formation in the North China craton. J Asian Earth Sci 24: 523–545

Wu FY, Zhao GC, Sun DY, Wilde SA, Yang JH (2007) The Hulan group: its role in the evolution of the central Asian Orogenic Belt of NE China. J Asian Earth Sci 30:542–556

Wu FY, Sun DY, Ge WC, Zhang YB, Grant ML, Wilde SA, Jahn BM (2011a) Geochronology of the Phanerozoic granitoids in northeastern China. J Asian Earth Sci 41:1–30

Wu HY, Zhang LC, Wan B, Chen ZG, Xiang P, Pirajno F, Du AD, Qu WJ (2011b) Re–Os and $^{40}Ar/^{39}Ar$ ages of the Jiguanshan porphyry Mo deposit, Xilamulun metallogenic belt, NE China, and constraints on mineralization events. Mineral Deposita 46:171–185

Xiao WJ, Windley BF, Hao J, Zhai MG (2003) Accretion leading to collision and the Permian Solonker suture, Inner Mongolia, China: termination of the central Asian orogenic belt. Tectonics 22

Xiao WJ, Windley BF, Huang BC, Han CM, Yuan C, Chen HL, Sun M, Sun S, Li JL (2009) End-Permian to mid-Triassic termination of the accretionary processes of the southern Altaids: implications for the geodynamic evolution, Phanerozoic continental growth, and metallogeny. Int J Earth Sci 98:1189–1217

Zarman RE, Haines SM (1988) The plumbotectonic model for Pb isotopic systematics among major terrestrial reservoirs: a case for bidirectional transport. Geochim Cosmochim Acta 52:1327–1339

Zeng QD, Liu JM, Zhang ZL, Chen WJ, Zhang WQ (2011) Geology and geochronology of the Xilamulun molybdenum metallogenic belt in eastern Inner Mongolia, China. Int J Earth Sci 100:1791–1809

Zeng QD, Yang JH, Liu JM, Chu SX, Duan XX, Zhang ZL, Zhang WQ, Zhang S (2012) Genesis of the Chehugou Mo-bearing granitic complex on the northern margin of the North China craton: geochemistry, zircon U–Pb age and Sr-Nd-Pb isotopes. Geol Mag 149:753–767

Zeng QD, Sun Y, Duan XX, Liu JM (2013) U–Pb and Re–Os geochronology of the Haolibao porphyry Mo–Cu deposit: China Office of Nuclear Energy, implications for a late Permian tectonic setting. Geol Mag 150:975–985

Zeng QD, Yang JH, Zhang ZL, Liu JM, Duan XX (2014) Petrogenesis of the Yangchang Mo-bearing granite in the Xilamulun metallogenic belt: China Office of Nuclear Energy, geochemistry, zircon U–Pb ages, and Sr–Nd–Pb isotopes. Geol J 49:1–14

Zhang LC, Wu HY, Wan B, Chen ZG (2009a) Ages and geodynamic settings of Xilamulun Mo–Cu metallogenic belt in the northern part of the North China craton. Gondwana Res 16:243–254

Zhang SH, Zhao Y, Song B, Hu JM, Liu SW, Yang YH, Chen FK, Liu XM, Liu J (2009b) Contrasting late carboniferous and late Permian–middle Triassic intrusive suites from the northern margin of the North China craton, geochronology, petrogenesis, and tectonic implications. Geol Soc Am Bull 121:181–200

Zhao Y, Chen B, Zhang SH, Liu JM, Hu JM, Liu J, Pen JL (2010) Pre-Yanshanian geological events in the northern margin of the North China craton and its adjacent areas. Geol China 37:900–915 In Chinese with English abstract

Zhou XH, Zhang GH, Yang JH, Chen WJ, Sun M (2001) Sr–Nd–Pb isotope mapping of late Mesozoic volcanic rocks across northern margin of North China craton and implications to geodynamic processes. Geochimica 30:10–23 In Chinese with English abstract

Zhu LM, Zhang GW, Guo B, Lee B, Gong HJ, Wang F (2010) Geochemistry of the Jinduicheng Mo-bearing porphyry and deposit, and its implications for the geodynamic setting in East Qinling, P.R. China. Chem Erde 70:159–174

Zindler A, Hart SR (1986) Chemical geodynamics. Earth Planet Sci Lett 14:493–571